

***UrbClim* – a fast urban boundary layer climate model**

Koen De Ridder, Dirk Lauwaet, Bino Maiheu

VITO – Flemish Institute for Technological Research, Mol, Belgium

Corresponding author:

Koen De Ridder

VITO

Boeretang 200 B-2400 Mol

BELGIUM

email: koen.deridder@vito.be

Abstract

We present a new urban climate model, further referred to as *UrbClim*, designed to cover agglomeration-scale domains at a spatial resolution of a few hundred metres. This model is composed of a land surface scheme containing simple urban physics, coupled to a 3-D atmospheric boundary layer module. In the land surface scheme, urban terrain is represented as an impermeable slab with appropriate parameter values for albedo, emissivity, and aerodynamic and thermal roughness length, and accounting for anthropogenic heat fluxes. The *UrbClim* model is subject to several validation exercises, using observations from Toulouse (France), Ghent and Antwerp (Belgium), and Bilbao (Spain), and considering turbulent energy fluxes, wind speed, and urban-rural temperatures. Despite its simplicity, *UrbClim* is found to be of the same level of accuracy than more sophisticated models, including for the complex terrain characterizing the Bilbao area. At the same time, it is faster than high-resolution mesoscale climate models by at least two orders of magnitude. Because of that, the model is well suited for long time integrations, in particular for applications in urban climate projections.

1. Introduction

Climate modification by urbanisation ranks among the most significant manifestations of human impact on the environment. In particular, cities experience air temperatures in excess of rural values, with average night-time temperature differences of typically a few °C, but increasing to 7-8°C and more under favourable conditions. Because of this urban heat island (UHI) increment, cities are particularly vulnerable to heat waves. Gabriel and Endlicher (2011), in a recent study on Berlin, found that during heat waves, mortality rates were higher in the city, especially in its most densely built-up districts. Dousset et al. (2012) found that in Paris, during the heat wave of the Summer of 2003, areas exhibiting the highest remotely sensed night-time infrared surface temperature suffered the highest heat-related excess mortality. The UHI phenomenon also has considerable implications for air quality (Sarrat et al., 2006; Davies et al., 2007) and cooling energy demand (Short et al., 2009).

At the same time, climate projections indicate that the frequency, intensity, and duration of heat waves is very likely to increase (Schär et al., 2004; Diffenbaugh and Giorgi, 2012), and that in the future cities may become more often exposed to extreme heat stress (IPCC, 2012). Urban climate modelling is increasingly considered a relevant tool for the evaluation of the impact and efficiency of urban (infrastructural) design measures aiming at the improved climate resilience of cities.

The increasing awareness of the vulnerability of urban areas to climate extremes, together with the increasing share of humans living in cities, has incited an increasing amount of research on urban climate processes. Over the past decades, numerical schemes of varying complexity have been developed to represent urban surface physics in atmospheric models. A large number of these urban surface schemes was recently evaluated in an international intercomparison study (Grimmond et al., 2010, 2011; Best and Grimmond, 2013). One of the principal, and striking, conclusions of this study was that simple models perform as well as more complex ones. Other workers similarly concluded that, for given a model, reducing complexity, e.g., in terms of the number of facets used to represent the urban canopy geometry, generally yields no loss of accuracy (Porson et al., 2009; Ikeda and Kusaka, 2010; Chemel and Sokhi, 2012).

Urban surface energy balance models have been implemented in mesoscale atmospheric models to simulate local climate features such as the urban heat island (Baklanov et al., 2008a). Yet, most studies have been restricted to fairly short periods, focusing on validation and on gaining an enhanced insight into relevant processes (e.g., Sarkar and De Ridder, 2011; Chemel and Sokhi, 2012; Wouters et al., 2013). The computation intensive character of coupled mesoscale-urban models has been a limiting factor for conducting long-term simulations. The main issue is that urban-scale simulations require a horizontal spatial resolution of the order of a kilometre or better, and at this resolution mesoscale models become exceedingly slow because of numerical stability constraints imposed on the time increment. Long model integrations therefore are difficult to achieve unless massive computational resources are available. This limitation has seriously hampered the use of mesoscale urban climate models in establishing long-term urban climate projections.

In this paper we present a simple, and therefore fast, but at the same time fairly accurate alternative for the traditional computation-intensive urbanized mesoscale climate models. This new model (*UrbClim*) is based on an existing land surface scheme containing a bulk parameterisation of the urban surface energy balance, coupled to a 3-D atmospheric boundary layer scheme.

The targeted spatial scale is that of an urban agglomeration and its nearby rural surroundings, generally yielding model domains a few tens of kilometres wide. Our approach is not aimed at an improved representation of urban surface processes. Rather, we propose a simple scheme, fast enough to allow model integrations covering tens of Summer seasons, while maintaining a satisfactory level of accuracy. Moreover, our approach specifies land surface parameters from generic and routinely available data sets, to allow an easy, fast, and consistent configuration of new urban domains.

It should be noted that other fast and accurate approaches exist to calculate urban canopy layer climate using observations from nearby rural reference stations (see, e.g., Erell and Williamson, 2006; Bueno et al., 2013). The main difference with our approach is that *UrbClim* requires external forcing by a large-scale host model. In doing so, we reduce the dependence upon the availability of local reference data, as well as the need to parameterize (or otherwise estimate) meteorological variables that are not measured routinely, such as incoming radiative fluxes. Last but not least, embedding our model within a large-scale host model entails the possibility of forcing *UrbClim* with climate projections generated by Global or Regional Climate Models, thus allowing urban climate projections.

The remainder of this paper is organized as follows. In Section 2, an overview is given of the urban surface energy balance and the atmospheric boundary layer modules contained in *UrbClim*. Section 3 presents the results of validation studies carried out over the cities of Toulouse (France), Ghent and Antwerp (Belgium), and Bilbao (Spain). Section 4 presents the conclusions.

2. Model description

The urban boundary layer climate model described below, and which will further be referred to as *UrbClim*, consists of a land surface scheme containing simplified urban physics, coupled to a 3-D atmospheric boundary layer module. The latter is tied to synoptic-scale meteorological fields through the lateral and top boundary conditions, to ensure that the synoptic forcing is properly taken into account.

2.1 Surface energy balance parameterisation

The land surface scheme is based on the soil-vegetation-atmosphere transfer scheme described in De Ridder and Schayes (1997). The vegetation- and soil-related processes are largely the same as in the original scheme, but the latter was extended to account for urban surface physics. Even though some aspects of the urban features have been previously described and used in De Ridder et al. (2012), no full account of the urban surface scheme is available, hence below we provide a complete description. We also include a description of the non-urban (soil and vegetation) parameterisations, but there the emphasis is on those aspects that differ from the original scheme. A graphic representation of the urban surface scheme is presented in Figure 1.

Each surface grid cell of the model is composed of portions of vegetation, bare soil, and urban surface cover, each with its own fraction, which is denoted by ϕ_u , ϕ_v , and ϕ_s , respectively. Although the model employs aggregated values for both the aerodynamic (z_0) and the thermal (z_{0t}) roughness

length parameters, each of the surface types within a grid cell has its own energy balance and corresponding temperature.

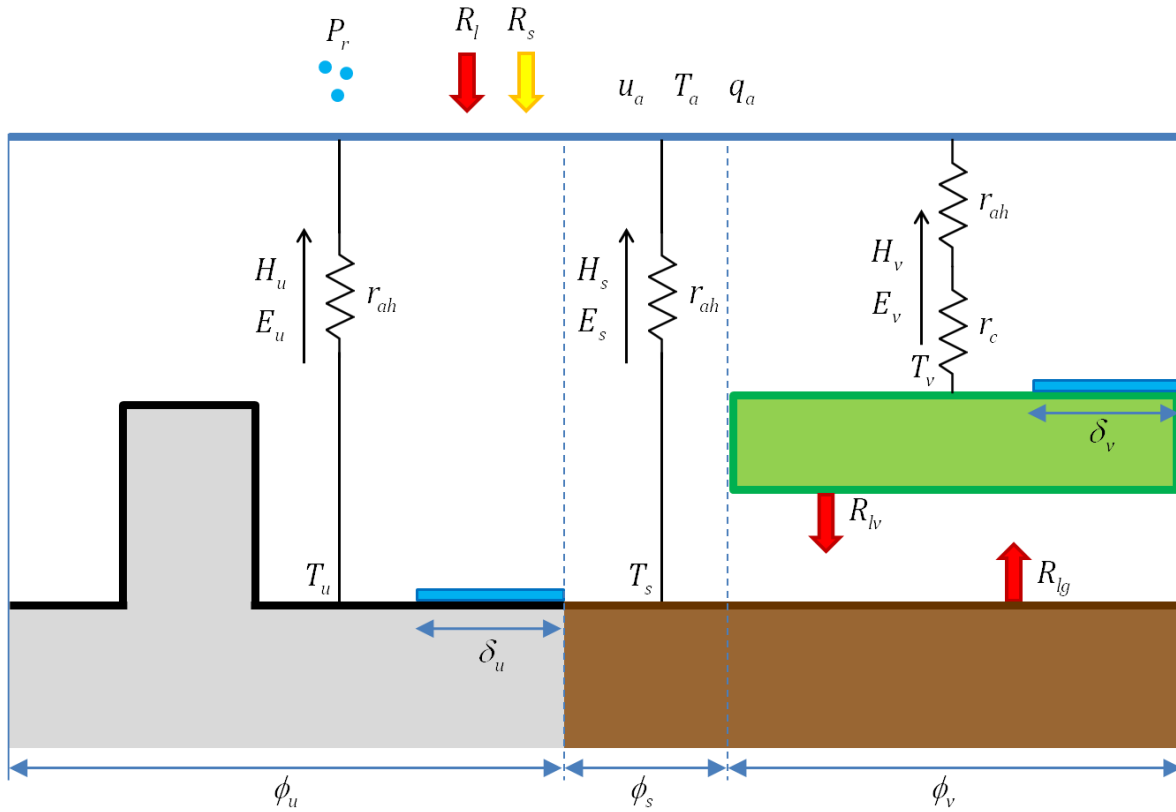


Figure 1. Schematic representation of the urban surface scheme, showing the urban slab (grey) co-existing with vegetation and bare soil fractions. The symbols contained in this diagram are explained in the main text (Section 2.1).

The ‘urbanisation’ of the original scheme was accomplished in a rather simple way, by representing the urban surface as a rough impermeable slab, with appropriate values for the albedo, emissivity, thermal conductivity and volumetric heat capacity (see below). The main feature of the extension of the scheme is the inclusion of a parameterisation of the inverse Stanton number,

$$kB^{-1} \equiv \ln\left(\frac{z_0}{z_{0t}}\right), \quad (1)$$

with $k \approx 0.4$ von Kármán’s constant. In contrast to homogeneously vegetated surfaces, which contain porous-rough obstacles and are characterised by values of $kB^{-1} \approx 2$, urban areas, which are composed of bluff-rough obstacles, exhibit much larger values (Garratt, 1992; Voegt and Grimmond, 2000; Kanda et al., 2007; Sugawara and Narita, 2009; De Ridder et al., 2012). The associated very low z_{0t} values strongly inhibit the turbulent transfer of heat from the urban substrate to the atmosphere, so that a relatively large share of the available radiant surface energy flux is converted to storage heat rather than to turbulent sensible heating of the atmosphere. This, together with the typically high values of thermal inertia of urban materials, leads to the large storage heat flux values typically observed (or estimated as a residual of the surface energy balance) over urban areas (Piringer et al., 2007). A particular feature of our model is that it accounts for the roughness sub-layer (Garratt,

1992) in the calculation of the surface energy fluxes, using analytic relations described in De Ridder (2010).

Since, within surface grid cells, vegetation and bare soil are allowed to co-exist with urban land cover, the aggregated kB^{-1} value is calculated following a suggestion by Kanda et al. (2007), as the weighted average of urban and non-urban contributions, i.e.,

$$kB^{-1} = \phi_u kB_u^{-1} + (1 - \phi_u) kB_v^{-1}, \quad (2)$$

with the non-urban value set at

$$kB_v^{-1} = 2.0 \quad (3)$$

as proposed by Garratt (1992), and with urban values being specified according

$$kB_u^{-1} = 1.29 \text{Re}_*^{0.25} - 2.0, \quad (4)$$

which is the parameterization by Brutsaert (1975) for bluff-rough surfaces (e.g., buildings), but with modified coefficients as recommended by Kanda et al. (2007). This expression is based on the roughness Reynolds number $\text{Re}_* = u_* z_0 / \nu$, with u_* the friction velocity, and $\nu = 1.461 \cdot 10^{-5} \text{ m}^2 \text{ s}^{-1}$ the kinematic viscosity of air.

While most other urban surface exchange models provide some canopy level detail, by decomposing the urban fabric into roof, wall and road facets, we have chosen to establish *UrbClim* on the simpler kB^{-1} -based (bulk) approach as described above. There are several reasons which have led to this choice.

For one, urban canopy models need to specify transfer coefficients between the building facets and the canopy air. Many models, also recent ones, rely on fairly ancient parameterizations, e.g., by Jürges (1924) (see, e.g., Ikeda and Kusaka, 2010; Pillai and Yoshie, 2013), or Rowley et al. (1930) (used in, e.g., Masson, 2000; Oleson et al., 2008). Efforts in this field are on-going (Defraeye et al., 2010; Chen et al., 2012), but Hagishima et al. (2005) ascertain that “our overall understanding of the convective heat transfer coefficients remains too low for accurate modelling of urban climate”.

Whereas these wall transfer coefficients were established by means of scale experiments, the kB^{-1} -based heat transfer coefficients in *UrbClim* were obtained from a series of real-world experiments that we conducted on actual cities, using remotely sensed surface thermal infrared temperature (De Ridder, 2006; De Ridder et al., 2008; De Ridder et al., 2012). While doing so entails disregarding certain physical processes occurring within the urban canopy, our approach at least has the merit that it is based on observations from actual urban areas, rather than that it has to rely on scale model experiments. Moreover, it has been shown that the use of the kB^{-1} framework is consistent with Monin-Obukhov similarity theory (Kanda et al., 2007).

Finally, there is another reason for using the simpler kB^{-1} approach, and which has to do with the intentionally generic character of *UrbClim*. Indeed, since we want the model to be easily configurable for any city, use has to be made of land cover data sets with an extensive geographical coverage, such as e.g. the CORINE land cover data for Europe (see below). When it comes to providing detail regarding urban surfaces, the information in such data sets is at best scanty. So, even though

detailed urban canopy models may in principle be the more accurate, the lack of suitable data to specify the required canopy characteristics (geometrical, material constants, etc...) is a considerable limitation.

The land surface scheme of *UrbClim* employs stability-dependent profile functions from surface layer similarity theory (Garratt, 1992) with, additionally, the inclusion of roughness sublayer effects as in De Ridder (2010),

$$u_a = \frac{u_*}{k} \left[\ln \left(\frac{z_a}{z_0} \right) - \Psi_M \left(\frac{z_a}{L} \right) + \Psi_M \left(\frac{z_0}{L} \right) + \Psi_M^* \left(\frac{z_a}{L}, \frac{z_a}{z_*} \right) \right] \left(\equiv \frac{u_*}{k} F_M \right) \quad (5)$$

$$T_a - T_0 = \frac{\theta_*}{k} \left[\ln \left(\frac{z_a}{z_0} \right) + kB^{-1} - \Psi_H \left(\frac{z_a}{L} \right) + \Psi_H \left(\frac{z_0}{L} \right) + \Psi_H^* \left(\frac{z_a}{L}, \frac{z_a}{z_*} \right) \right] \left(\equiv \frac{\theta_*}{k} F_M \right).$$

In these expressions, which are solved for $\zeta = z_0/L$ iteratively through the formation of the bulk Richardson number (see, e.g., Arya, 2002), L is the Obukhov length, u_a and T_a are the magnitude of the wind vector and temperature at a reference height z_a above the displacement height (which is taken here as the first model level in the atmosphere above the ground, see Section 3), θ_* is the turbulent temperature fluctuation scale, and T_0 is the aerodynamic surface temperature,

$$T_0 = \phi_u T_u + \phi_v T_v + \phi_s T_s, \quad (6)$$

with T_u , T_v , and T_s the surface temperatures of, respectively, the urban surface cover, vegetation, and bare soil portions.

In the above expressions, Ψ_M and Ψ_H are the integral stability functions for momentum and heat, respectively. In unstable conditions ($\zeta < 0$), we use the Paulson (1970) expressions, and in stable conditions ($\zeta > 0$) the functions proposed by Cheng and Brutsaert (2005), which, in a comparative study by Ghuo and Zhang (2007), were recommended as the most suitable for a large range of stably stratified conditions, including very stable ones. Also, they found this parameterisation to perform well for high ratios of z_0/z_{0t} , which is of obvious relevance here. The above expressions also employ the roughness sub-layer correction functions Ψ_M^* and Ψ_H^* as defined in De Ridder (2010). These functions represent the effect of the roughness sub-layer on the profile functions as proposed in Physick and Garratt (1995), but using analytic expressions rather than numerical integration. These functions make use of the roughness sub-layer depth $z_* \approx 16.7 z_0$ as a scaling variable.

Once the Obukhov length L known from the iterative solution of (5), the turbulent aerodynamic resistances for momentum and scalar quantities can be specified as, respectively,

$$r_{am} = \frac{1}{k^2 u_a} F_M^2 \quad (7)$$

$$r_{ah} = \frac{1}{k^2 u_a} F_M F_H,$$

with the functions F_H and F_M as defined in (5). It should be noted that, even though the land surface model considers separate energy and water balance formulations for urban, vegetation, and soil

surfaces occurring within a grid cell, turbulent transfer as it is represented by r_{ah} is defined at the level of the grid cell as a whole. The reason for doing so is that (see Section 3) we do consider model applications with spatial resolutions of the order of a few hundred metres, and it is fair to assume that on this scale turbulent intensities, as represented by the aerodynamic resistances, are fairly homogenous.

The energy fluxes of the purely **urban** portion of a grid cell (indicated with subscript u) are specified as follows:

$$\begin{aligned}
 R_{nu} &= (1 - \alpha_u)R_s + \varepsilon_u (R_l - \sigma T_{u1}^4) \\
 H_u &= \rho_a c_p \frac{T_{u1} - T_a}{r_a} \\
 LE_u &= \rho_a L_v \delta_u \frac{q_{u1} - q_a}{r_a}.
 \end{aligned} \tag{8}$$

In the expression for net radiation (R_{nu}), α_u and ε_u represent the albedo and emissivity of the urban substrate, $\sigma = 5.67 \cdot 10^{-8} \text{ W m}^{-2} \text{ K}^{-4}$ is the Stefan-Boltzman constant, and T_{u1} is the urban surface temperature. The expression for latent heat (LE_u) contains the specific humidity of the urban surface, which is defined as the saturated value at temperature T_{u1} . The latent heat flux formula also contains the fractional surface wetness δ_u , which accounts for water stored on the urban substrate, and which depends on the amount w_{su} (in kg m^{-2}) of water stored as

$$\delta_u = \delta_{u0} \left(\frac{w_{su}}{w_{su0}} \right)^{2/3}, \tag{9}$$

with $\delta_{u0} = 0.14$ the fraction of wet surface occurring at the maximum of urban water storage capacity, and with a maximum storage capacity of $w_{su0} = 1.17 \text{ kg m}^{-2}$, both parameters having been estimated recently by Wouters et al. (2014). The amount of water stored is itself governed by the prognostic equation

$$\frac{\partial w_u}{\partial t} = P_r - E_u, \tag{10}$$

with P_r the precipitation rate, and E_u the evaporation flux as specified in (8).

The urban substrate is represented as a massive slab, which is discretized in six vertical layers with thickness (from top to bottom) of 0.005, 0.02, 0.07, 0.3, 0.6, and 1.0 m. The temperature evolution of each layer i ($= 1, \dots, 6$) is governed by

$$\begin{aligned}
 C_{u,i} \frac{\partial T_{u,i}}{\partial t} &= \frac{F_{u,i-1} - F_{u,i}}{d_i} \\
 F_{u,i} &= -\lambda_{i,i+1} \frac{T_{u,i+1} - T_{u,i}}{(d_i + d_{i+1})/2},
 \end{aligned} \tag{11}$$

with volumetric heat capacity $C_{u,i} = 2 \times 10^6 \text{ J m}^{-3} \text{ K}^{-1}$, and thermal conductivity $\lambda_{i,i+1} = 2 \text{ W m}^{-1} \text{ K}^{-1}$, in line with values generally found in the literature for urban areas (see, e.g., Oke, 2002; Pielke, 2002).

Moreover, d_i denotes the layers' thickness and $F_{u,i}$ represents the flux of heat occurring between adjacent layers.

At the lower boundary, we impose a vanishing heat flux, and at the upper boundary

$$F_{u,0} = R_{nu} - H_u - LE_u. \quad (12)$$

Equation (11) is solved using a forward-in time explicit numerical scheme, using an appropriate time step for this diffusion equation to obtain a stable solution (see, e.g., Pielke, 2002). For the upper slab layer, where evaluation of numerical stability requirements are somewhat complicated by the presence of the surface-atmosphere energy fluxes as shown in (12), a maximum allowable stable time increment as derived in the Appendix is used.

Finally, the model accounts for anthropogenic heating, following the approach of Demuzere et al. (2008), which is based on the specification of a 'reference' anthropogenic heat flux in grid cells featuring full (i.e., 100%) urban land cover, and subsequently disaggregating this reference flux spatially and temporally. The spatial disaggregation is achieved by scaling with the actual percentage urban land cover occurring in a given grid cell, and the temporal disaggregation is based on a diurnal temporal profile, yielding higher flux values during the day and less at night. As the method described in Demuzere et al. (2008) was developed for Marseille (France), when considering other cities, reference anthropogenic heat flux values (i.e., corresponding to 100% urban land cover) are scaled up (or down) from the Marseille value by means of the night-time radiance values observed by the Defense Meteorological Satellite Program – Operational Line Scanner (DMSP-OLS) (Elvidge et al., 1999), data of which can be obtained from the U.S. National Geophysical Data Center (ngdc.noaa.gov).

The anthropogenic heat flux is directly added to the surface air as an extra sensible heat flux. This approach is also followed by Fan and Sailor (2005), following work by Sailor and Fan (2004), demonstrating that the simulated temperature profiles are only slightly affected by the actual method of including the anthropogenic heat flux (i.e., either adding it as a direct flux to the atmosphere, or including it as a substrate heating term).

The energy fluxes for the **vegetation**-only part of a grid cell (subscripts v) are specified as follows:

$$\begin{aligned} R_{nv} &= (1 - \alpha_v)R_s + \varepsilon_v(R_l - \sigma T_v^4) + \sigma(T_{s1}^4 - T_v^4) \\ H_v &= \rho_a c_p \frac{T_v - T_a}{r_a} \\ LE_v &= \rho_a L_v \left[\delta_v \frac{q_v - q_a}{r_a} + (1 - \delta_v) \frac{q_v - q_a}{r_a + r_c} \right]. \end{aligned} \quad (13)$$

In the expression for the vegetation's net radiation (R_{nv}), α_v and ε_v are the albedo and emissivity, T_v and T_{s1} are the temperature of the vegetation and upper soil layer, respectively. Remark that the last term in this expression represents the net radiation arising from exchange of long-wave radiation between vegetation and the underlying soil. In the expression for the sensible heat flux (H_v), ρ_a represents air density, and $c_p = 1004 \text{ J kg}^{-1} \text{ K}^{-1}$ is the specific heat at constant pressure for air. Finally, in the expression for the latent heat flux (LE_v), $L_v = 2.5 \times 10^6 \text{ J kg}^{-1}$ is the latent heat of vaporization, δ_v is

the fractional wetness of the leaves (see below), q_v and q_a are the specific humidity of the vegetation (assumed saturated at its temperature T_v) and the air, and r_c is the stomatal resistance, which is parameterized as

$$r_c = \frac{r_{c0}}{L_e} \left(1 - \frac{\psi_v}{\psi_{vc}} \right)^{-1}, \quad (14)$$

with r_{c0} the vegetation type-dependent unconstrained stomatal resistance per unit LAI, L_e the effective LAI as defined in De Ridder (1997), ψ_v the leaf water potential (see below), and ψ_{vc} a critical threshold value for the latter, below which the stomata shut close. More details regarding this r_c -parameterization are provided in De Ridder and Schayes (1997).

Leaf water potential is diagnosed as a function of internal leaf water content, denoted w_v , using the Höfler-Thoday relations (Jones, 1992)

$$\psi_v = \psi_c \frac{w_{v0} - w_v}{w_{v0} - w_{vc}}, \quad (15)$$

with w_{v0} the maximum internal water storage capacity (set to 0.2 kg m⁻² per unit LAI), and w_{vc} the lower, critical, threshold, at which the leaf water potential reaches the critical value ψ_{vc} . Leaf water content is itself governed by the prognostic conservation equation

$$\frac{\partial w_v}{\partial t} = F_r - E_{tr}, \quad (16)$$

with F_r the water flux arising from root water uptake, and E_{tr} the vegetation transpiration flux. The leaf internal water storage is constrained to the range $w_{vc} < w_v < w_{v0}$.

Apart from internal leaf water, the model also accounts for water stored *on* the leaves (denoted w_{sv}) upon interception of precipitation, and its subsequent evaporation, using

$$\frac{\partial w_{sv}}{\partial t} = P_r - E_{dir}, \quad (17)$$

with

$$E_{dir} = \rho_{av} \delta_v \frac{q_v - q_a}{r_a}, \quad (18)$$

the evaporation of the stored water is proportional to the leaf wetness, which is itself specified as a function of the stored water using

$$\delta_v = \left(\frac{w_{sv}}{w_{sv0}} \right)^{2/3}, \quad (19)$$

with w_{sv0} the maximum storage capacity, which is assigned a value of 0.2 kg m⁻² per unit LAI.

The components of the vegetation's energy balance (13) are used to update vegetation temperature,

$$C_v \frac{\partial T_v}{\partial t} = R_{nv} - H_v - LE_v, \quad (20)$$

with C_v the heat capacity of the leaves, which is set to that of 0.2 kg m^{-2} water per unit LAI, and t is time. Again, as was the case for the temperature evolution equation of the urban slab's upper layer, we employ the stability criterion derived in the Appendix to constrain the time step in the numerical solution of (20).

The energy balance of the **soil-only** (subscripts s) portion of a grid cell, expressed per unit of exposed (i.e., not lying underneath vegetation) soil surface, is written as follows:

$$\begin{aligned} R_{ns} &= (1 - \alpha_s) R_s + \varepsilon_s (R_l - \sigma T_{s1}^4) + \sigma (T_v^4 - T_{s1}^4) \phi_v / \phi_s \\ H_s &= \rho_a C_p \frac{T_{s1} - T_a}{r_a} \\ LE_s &= \rho_a L_v \frac{q_{s1} - q_a}{r_a}. \end{aligned} \quad (21)$$

In the expression for net radiation (R_{ns}), α_s and ε_s represent the albedo and emissivity of the soil. The factor ϕ_s / ϕ_v in the last term is required to account for the fact that the soil energy fluxes are expressed per unit of *exposed* soil only. The expression for latent heat (LE_s) contains the specific humidity of the soil surface, which is defined as the saturated value at the soil's upper layer temperature T_{s1} . Evaporation from the soil is constrained by the maximum moisture flux that can be sustained by the soil at a given volumetric moisture content, as in De Ridder and Schayes (1997).

The evolution of the temperature profile in the soil is calculated using the same heat diffusion equations (11) as those used for the urban slab. The main difference is that, for soil, the volumetric heat capacity and thermal conductivity are functions of soil moisture content, as in De Ridder and Schayes (1997). Moreover, given that the energy fluxes (21) are expressed per unit of exposed soil surface, while the soil does also extend under the vegetation, the upper boundary condition becomes

$$F_{s,0} = \frac{\phi_s}{\phi_v + \phi_s} (R_{ns} - H_s - LE_s), \quad (22)$$

i.e., the storage heat which results as a residual from the balance of the components appearing in (21) has to be 'diluted' by an appropriate factor $\phi_s / (\phi_s + \phi_v)$.

Finally, water transport in the soil is described by means of Richards' equation (Garratt, 1992), accounting for infiltration of rain water in the soil and the uptake of soil water by plant roots. Here also, the reader is referred to De Ridder and Schayes (1997) for more details.

Note that the bulk urban surface scheme described in this section, when used previously within the mesoscale meteorological model ARPS (Xue et al., 2000), has been demonstrated good skill in reproducing observed surface energy fluxes (Demuzere et al., 2008), radiometric surface temperatures (De Ridder, 2006; De Ridder et al., 2008; De Ridder et al., 2012), and urban-rural 2-m air temperature differences (Van Weverberg et al., 2008; Sarkar and De Ridder, 2011; Wouters et al., 2013).

The input variables required by the land surface scheme are: wind speed (u_a), temperature (T_a) and specific humidity (q_a) at a reference level (z_a) close to the surface, which is typically at a height of ten to a few tens of metres. These quantities are taken from values simulated in the atmospheric boundary layer model (Section 2.2) or, if run in off-line mode, could also be specified from observations. Moreover, the land surface scheme requires the specification of downwelling short- (R_s) and longwave (R_l) radiation fluxes, and precipitation (P_r). These latter variables are directly taken from the large-scale driving atmospheric model, since our atmospheric boundary layer model (Section 2.2) contains no internal representation of cloud, precipitation, nor radiation. The output generated by the land surface scheme consists of the turbulent fluxes of sensible and latent heat, and momentum. These fluxes serve as lower boundary conditions for the atmospheric boundary layer model, which will be described next.

2.2 Atmospheric boundary layer model

As mentioned before, a full mesoscale model at kilometre-scale resolution is very costly in terms of the time required to perform a simulation. Therefore, we developed a very simple 3-D model of the lower atmosphere, comprising the atmospheric boundary layer and typically extending to a height of a few kilometres. This model is represented by conservation equations for horizontal momentum (considering zonal and meridional wind speed components u and v , respectively), potential temperature (θ), specific humidity (q), and mass (involving the vertical wind speed component w),

$$\begin{aligned}
\frac{\partial u}{\partial t} + u \frac{\partial u}{\partial x} + v \frac{\partial u}{\partial y} + w \frac{\partial u}{\partial z} &= -\frac{1}{\rho_0} \frac{\partial P_0}{\partial x} + fv - \frac{\partial}{\partial z} (\overline{u'w'}) \\
\frac{\partial v}{\partial t} + u \frac{\partial v}{\partial x} + v \frac{\partial v}{\partial y} + w \frac{\partial v}{\partial z} &= -\frac{1}{\rho_0} \frac{\partial P_0}{\partial y} - fu - \frac{\partial}{\partial z} (\overline{v'w'}) \\
\frac{\partial \theta}{\partial t} + u \frac{\partial \theta}{\partial x} + v \frac{\partial \theta}{\partial y} + w \frac{\partial \theta}{\partial z} &= -\frac{\partial}{\partial z} (\overline{w'\theta'}) \\
\frac{\partial q}{\partial t} + u \frac{\partial q}{\partial x} + v \frac{\partial q}{\partial y} + w \frac{\partial q}{\partial z} &= -\frac{\partial}{\partial z} (\overline{w'q'}) \\
\frac{\partial u}{\partial x} + \frac{\partial v}{\partial y} + \frac{\partial w}{\partial z} &= 0.
\end{aligned} \tag{23}$$

In these expressions, x , y , and z denote the zonal, meridional and vertical coordinate variables, respectively. Since the intended focus of our model is on the lowest kilometre of the atmosphere, we employ the incompressible continuity equation, as shown by the last expression in (23). The Earth's rotation is accounted for through the Coriolis parameter $f = 2\Omega \sin \varphi$, with $\Omega \approx 7.29 \times 10^{-5} \text{ rad s}^{-1}$ the rotation rate and φ the latitude, for which we take the value at the centre of the domain. In the momentum equations, ρ_0 represents a reference air density and P_0 the pressure field. The latter is not calculated internally, but prescribed from the large-scale host model that provides the boundary conditions, hence only the synoptic-scale pressure gradient is accounted for. By doing so we avoid the complexities associated with a full mesoscale meteorological model. More importantly, it allows the use of much longer time increments in the numerical solver, and a lower model top (since no absorbing layer is required to damp gravity waves), hence making the model much faster.

The expressions between brackets in the right-hand side of (23) represent vertical turbulent fluxes. These are calculated using a classical gradient-diffusion analogue, based on

$$\overline{\chi'w'} = -K_\chi \frac{\partial \chi}{\partial z}, \quad (24)$$

with χ one of u, v, θ, q ; and K_χ the corresponding turbulent diffusion coefficient. Following Hong and Pan (1996), the turbulent vertical diffusion coefficient for scalar quantities in the mixing layer with height z_i is calculated as

$$K_H(z) = \frac{ku_*z}{\phi_H(z/L)} \left(1 - \frac{z}{z_i}\right)^2, \quad (25)$$

with the requirement that, in the argument of ϕ_H , z be smaller than $0.1 z_i$. Eq. (25) reduces to surface layer scaling for $z \ll z_i$, smoothly merging into the mixed-layer profile for larger z . A similar expression applies to the momentum diffusivity K_M , though using ϕ_M instead. The stability functions $\phi_{H(M)}$ are those corresponding to the integral stability functions $\Psi_{H(M)}$ specified in Section 2.1. The above expression is only valid within the mixing layer ($z < z_i$). Above this layer the turbulent diffusion coefficient is set to a fixed value of $1 \text{ m}^2 \text{ s}^{-1}$.

The mixing layer height z_i is determined by means of a bulk Richardson approach, following Sørensen et al. (1996), and based on the expression

$$\text{Ri}_B(z) = \frac{gz}{\theta_{v1}} \frac{\theta_v(z) - \theta_{v1}}{u^2(z) + v^2(z)}, \quad (26)$$

with $g = 9.8065 \text{ m s}^{-2}$ the gravitational acceleration, and $\theta_v = \theta (1+0.61q)$ the virtual potential temperature, the subscript '1' referring to values occurring at the first model level. The mixing layer height is obtained as the solution of $\text{Ri}_B(z_i) = \text{Ri}_{B,c} \approx 0.25$. Practically, z_i is calculated by means of (26), starting at the first level above the surface and gradually working upward until a layer is encountered where $\text{Ri}_B > \text{Ri}_{B,c}$. When that occurs, a linear interpolation is performed to obtain the actual value of z_i .

The numerical solution of the atmospheric conservation equations (23) is achieved using a finite difference scheme, based on an Arakawa C-grid discretisation (Pielke, 2002). The advection terms are written in flux-conservative form and solved using the Walcek (2000) scheme, which includes a flux limiter, ensuring a positive-definite solution. At every integration step, the maximum allowable magnitude of the time increment Δt_{\max} is calculated based on the Courant criterion, such that

$$\Delta t_{\max} = \Delta x / V_{\max}, \quad (27)$$

with Δx the horizontal grid resolution and V_{\max} the largest wind speed value occurring in the domain. This adaptive calculation of the time step ensures a fast and efficient integration.

At the model's inflow boundaries (i.e., at boundary cells where the external wind vector is pointing towards the inside of the domain), prognostic quantities are specified as values interpolated spatially and temporally from output fields of a large-scale atmospheric driving model. At outflow boundaries,

a zero-gradient condition is imposed, so as to allow perturbations to flow out of the domain freely. Vertical diffusion is solved using the Crank-Nicolson (1947) algorithm. At the lower (surface) boundary, the momentum, heat, and moisture fluxes are specified as those generated by the land surface scheme described in Section 2.1. At the model top, which is taken at a few kilometres height, values interpolated from the large-scale driving model are imposed. The specification, from the large-scale driving model, of the lateral and top boundary conditions, the synoptic-scale pressure gradient, and the downwelling radiation and precipitation fluxes, allows to account for the effect of synoptic weather on local climate, and defines the nesting of our urban boundary layer climate model within the large-scale host model.

When coupling *UrbClim* to a large-scale host model, a sufficient temporal resolution of the latter's forcing fields is required. Basically, the time step at which large-scale data are required should more or less resolve the diurnal cycle, hence a forcing time step of three hours or shorter is required. We will comment more on the availability of such data below.

The first model level is generally situated at 10 m or higher above the displacement height. Temperatures at a lower level are estimated diagnostically by extrapolation, using the profile functions specified in (5). While often temperature is required at the 2-m level, for urban surfaces, the vertical extrapolation is performed down to roof level, i.e., down to a height $z = h - d$ (recall that the model 'bottom' is placed at the displacement height d), and assuming that the resulting temperature is representative for the urban canyon as a whole, which is assumed homogeneously mixed. This homogeneous mixing assumption in the urban canopy layer is supported by several studies. Nakamura and Oke (1988) measured very slight air temperature gradients only through most of the urban canopy layer, as long as the considered location was not too close to a lateral surface. In their urban canopy model, Erell and Williamson (2006), make this same assumption. Also, measurements acquired in a street canyon in Basel (Switzerland) at different times of the day (Rotach et al., 2005) show little vertical temperature variation, and show that the top-of-canopy temperature is fairly representative of values lower down in the canopy. Finally, in a numerical experiment conducted with a computational fluid dynamics model on an idealized street canyon, Solazzo and Britter (2007) found the canyon air temperature to be spatially nearly uniform, apart from a thin near-wall thermal boundary layer.

The effects of terrain height on surface air temperature are accounted for by applying a lapse-rate based correction factor of 6.5 K km^{-1} to the simulated temperature fields. Terrain elevation data are taken from the GMTED2010 Dataset (Danielson and Gesh, 2011), which has a global coverage at a spatial resolution of approximately 250 m, and is available from the U.S. Geological Survey (topotools.cr.usgs.gov).

3. Model evaluation

The model described in Section 2 was applied to Toulouse (France), Ghent and Antwerp (Belgium), and Bilbao (Spain), and simulated quantities were compared to observed values. Because, apart from their location, the model domains share several aspects pertaining to their configuration, we describe these first.

The spatial distribution of land cover types, required for the specification of certain land surface parameters, was taken from the CORINE land cover data for Europe, which is available from the European Environment Agency (www.eea.europa.eu). The 44 CORINE land cover types were aggregated into a set of nine model types. A list of these, together with the land surface parameter values assigned to them, is given in Table 1.

Table 1. Overview of the land cover types used in UrbClim, and parameter values assigned to them. The left column gives the identifying acronym of each type, which corresponds to those used in Figures 2 and 6. The symbol α refers to the albedo, ε is emissivity, z_0 is the aerodynamic roughness length, and r_c is the unconstrained canopy resistance.

ID	type	α (-)	ε (-)	z_0 (m)	r_c (s m ⁻¹)
WTR	water	0.05	0.99	10 ⁻⁴	-
URC	high-dense urban	0.12	0.95	1.50	-
URD	low-dense urban	0.15	0.95	0.50	-
IND	industrial	0.15	0.95	0.30	-
GRS	grassland	0.20	0.98	0.05	100
CRP	cropland	0.20	0.98	0.10	100
SHR	shrubland	0.15	0.98	0.10	200
WDL	woodland	0.15	0.98	0.50	200
FOR	forest	0.15	0.98	1.20	200

The percentage urban land cover was specified using the Urban Soil Sealing raster data files distributed by the European Environment Agency. Maps of vegetation cover fraction (ϕ_v) were obtained from the Normalized Difference Vegetation Index (NDVI) acquired by the MODIS instrument on-board the TERRA satellite platform at a resolution of 250 m. These data are available from the Land Processes Distributed Active Archive Center of the U.S. Geological Survey (lpdaac.usgs.gov). Vegetation cover fraction was specified as a function of the NDVI using a linear relationship proposed by Gutman and Ignatov (1998), and then interpolated to the model grid. Model grid cells featuring exclusively non-urban land use types are divided into vegetation (fraction ϕ_v) and bare soil (the complementary fraction $1-\phi_v$). In the case of grid cells containing urban land use, the urban fraction as derived from the Soil Sealing data (see above) takes precedence over the NDVI-based fractional vegetation cover data in case both sum to over 100%. In case they sum to less than that, the remaining fraction is assigned to bare soil.

All domains were configured with 121×121 grid cells in the horizontal direction, using a spatial resolution of 250 m. Even though higher spatial resolutions might often be preferred, it should be kept in mind that our bulk surface transfer approach, in which the urban surface is represented in an aggregated way, inhibits the use of too high a spatial resolution, as from a certain point onwards large buildings become explicitly resolved, which is incompatible with the model's bulk approach. In case a higher level of spatial detail is required, an obstacle-resolving approach based on Computational Fluid Dynamics (CFD) modelling may be suited better. In any case, a resolution of 250 m is already considerably finer than what is customarily used in limited-area weather and climate modelling applied over cities, which generally employ resolutions of around 1 km or coarser. (In this context, it should be noted that Sobrino et al. (2012), based on the analysis of aerial thermal-infrared imagery over Madrid, concluded that a spatial resolution of the order of a few hundred metres resolves the detail at the city neighbourhood scale much better than a 1-km resolution.) Finally, in

our simulations, the 250 m resolution appeared to present a good trade-off between the resulting spatial detail and model execution speed.

The above-mentioned configuration yields model domains with a size of approximately 30 km which, for the medium-size cities considered here, was found to be appropriate. In the vertical direction, 20 levels were specified, with the first level 10 m above the displacement height, the resolution smoothly decreasing upward to 250 m at the model top located at 3 km height. This vertical discretisation closely matches that of the host model which, for this study, is the global operational model of the European Centre for Medium Range Weather Forecasting (ECMWF, data can be obtained from www.ecmwf.int).

In this configuration, and for all domains considered, the time required to complete a simulation of one month took approximately 10 hours on a single core of a Pentium Xeon 3.0 GHz processor. We compared this to the execution speed of full mesoscale models such as ARPS (Xue et al., 2000) and COSMO-CLM (Rockel et al., 2008), which are also run at our Institute. From that, it was estimated that for a given domain size, spatial resolution, and simulation length, *UrbClim* is faster by more than two orders of magnitude.

3.1 Toulouse

We ran our model for Toulouse, in the South of France, and which has a population of approximately 440,000 in the city, the wider urban agglomeration counting more than 1,200,000 inhabitants. The selected period consisted of the months of June-July 2004, which corresponds to the intensive observation period of the CAPITOUL campaign that took place in Toulouse in 2004-2005 (Masson et al., 2008). Figure 2 shows the land cover types and vegetation cover fraction of the simulation domain.

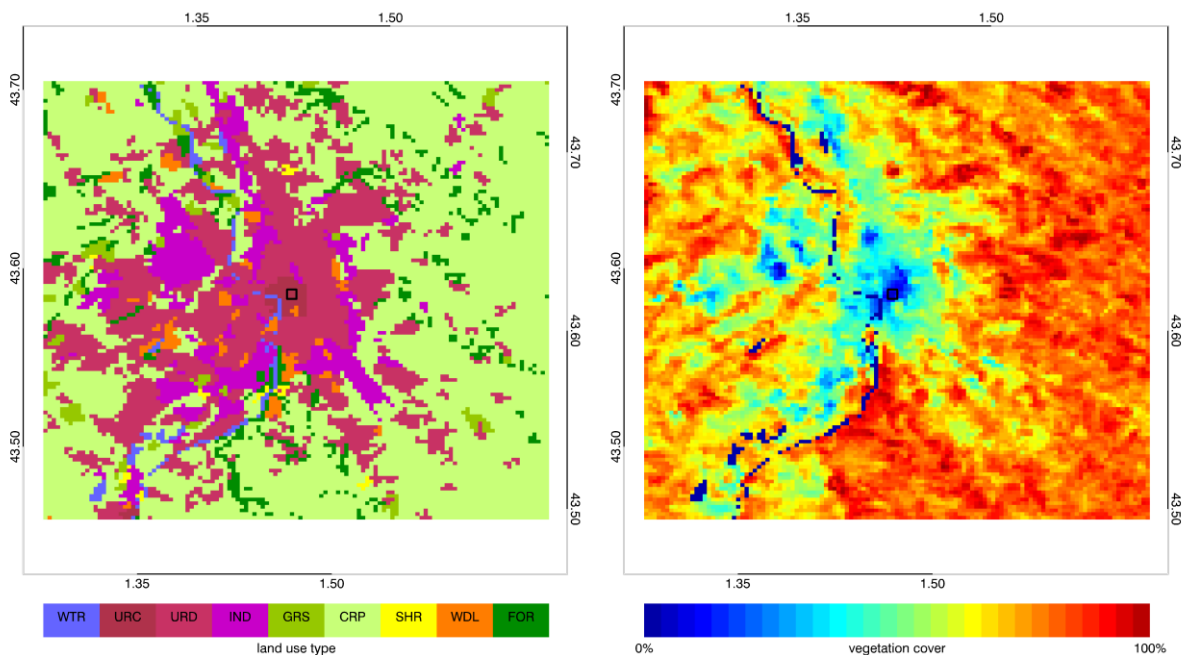


Figure 2. Spatial distribution of the dominant land cover type (left) and percentage vegetation cover (right) for the Toulouse modelling domain. The acronyms denoting the different land cover types are explained in Table 1.

For the validation we used energy flux data measured at a dense urban site in the downtown area of Toulouse on a 27.5 m high instrumented tower, itself mounted on a roof of a 20-m high building. Turbulent energy fluxes were measured with the eddy covariance technique, using a sonic Gill HS50 to acquire the turbulent fluctuations of the wind speed components and temperature, and a Licor 7500 to measure water vapour fluctuations. In order to compare measured turbulent fluxes with simulated values, the latter were spatially averaged over a 3×3 grid cell block centred on the position of the instrument tower, which is relatively close to the circular footprint area with radius 500 m around the measurement tower, which was used in earlier studies (Pigeon et al., 2007). Indeed, given the height of the eddy correlation instruments, they collect turbulent fluctuations that originate in source areas not located right below the measurement tower, and not even from within the model grid cell in which the experimental site is located. Note that using a mean flux source footprint area, as we do here, instead of the actual (time-dependent) footprint, has its limitations when comparing model output to the observed fluxes, as will be shown below.

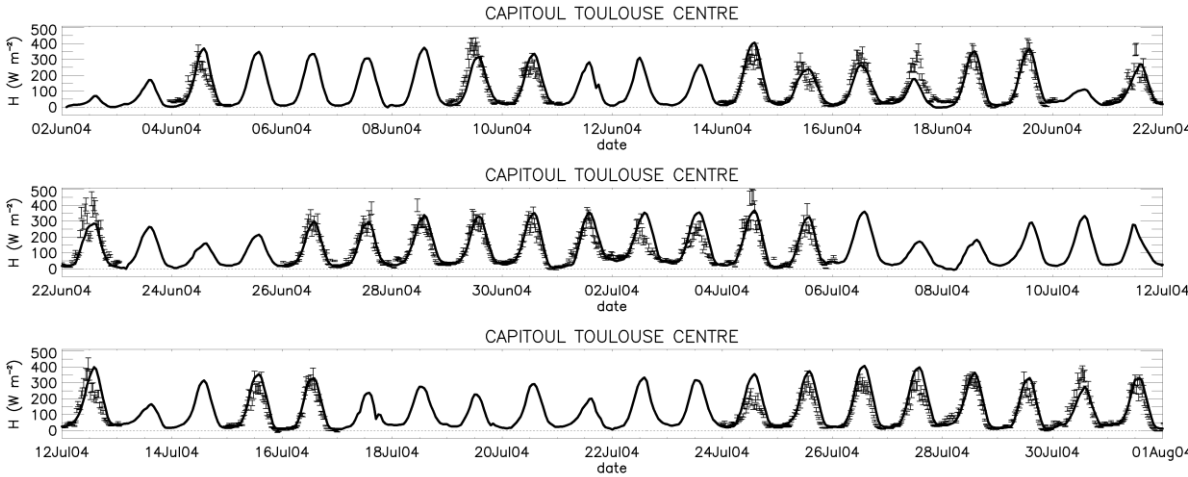


Figure 3. Simulated (solid line) versus observed (error flags) sensible heat flux for central Toulouse, June-July 2004.

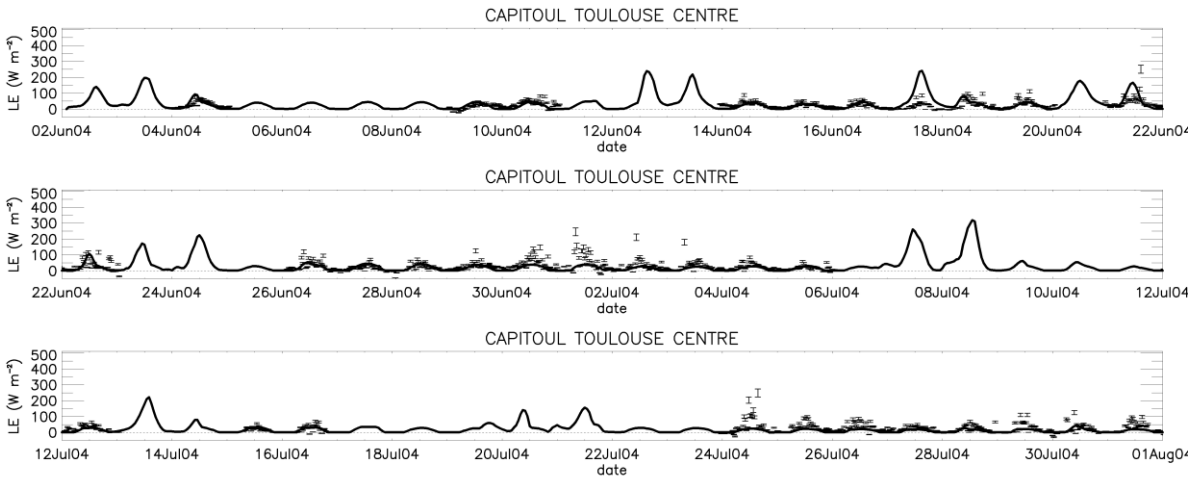


Figure 4. Simulated (solid line) versus observed (error flags) latent heat flux for central Toulouse, June-July 2004.

Figures 3 and 4 show time series of the observed and simulated sensible and latent heat fluxes for the considered two-month period. We assigned error bars with a magnitude of 10 and 15% of the instantaneous sensible and latent heat flux values, respectively, in accordance with results presented in Mauder et al. (2007) from an experimental inter-comparison study. The study period is characterized by rather high values of the sensible heat flux most of the time, with a diurnal amplitude of approximately 300 W m^{-2} , except on cloudy days. The latent heat flux is generally low, except during or shortly after precipitation, when it may reach several hundred W m^{-2} . In between rainy periods, there is a small residual latent heat flux with values up to a few tens of W m^{-2} , presumably caused by transpiring vegetation. Figure 3 shows that both the phase and diurnal amplitude of the simulated sensible heat flux match the observations fairly well. Especially, the observed night-time values of the simulated sensible heat flux, with slightly positive values, are reproduced correctly. This is important when considering the urban heat island effect, which reaches its highest intensity in the evening and early night.

Some discrepancies are to be noted, though. On 17 June, the model underestimates (overestimates) the sensible (latent) heat flux. This was traced back to the presence of rain in the ECMWF forcing data, while this rain was absent in the on-site measurements. Also, on 30 June and the subsequent days, as well as on e.g. 24 July, the observed latent heat flux is underestimated by the model. Since the on-site measurements do not show precipitation on these days, we believe the underestimation to be related to local surface heterogeneity, in particular the presence of the river 800 m to the West of the experimental site. Inspection of locally measured wind data revealed the prevalence of westerly winds during these days, which probably puts the flux source area over the river. Since in our approach (see above) we only account for a mean flux footprint area and not for the actual wind direction-dependent footprint, our model cannot reproduce the observed features. Some other, minor discrepancies could be traced back to the solar radiation being somewhat off in the ECMWF data compared to the in-situ measurements, e.g. the underestimated sensible heat flux on 30 July was found to be most likely associated to an underestimated downwelling shortwave radiation flux.

When compared to observed values, the simulated sensible heat flux exhibits a bias of 10 W m^{-2} , a root mean square error of 49 W m^{-2} , and a correlation coefficient of 0.91. To appreciate the performance of this simulation, we compare its error values with those obtained by other workers. Error statistics presented by Best and Grimmond (2012) are particularly interesting, as they consider time series of observed and simulated values which also cover two months, and since their results consider a large number (tens) of urban land surface schemes that participated in an inter-comparison study (Grimmond et al., 2010). In Best and Grimmond (2012), the data used to compare the models with consist of eddy correlation-based turbulent surface fluxes from Melbourne (Australia) which, as Toulouse, is characterized by a humid temperate climate. Both sites also exhibit similar mean diurnal cycles of the observed sensible heat flux, with mean daytime-maxima slightly below 300 W m^{-2} . Of course, given its location in the Southern hemisphere, we used the Melbourne results for the December-January period for comparison with our June-July results.

The root mean square error on the sensible heat flux of 49 W m^{-2} simulated for Toulouse with our model is smaller than any of the December-January values presented in Best and Grimmond (2012), which is in the range of 56 to 134 W m^{-2} , though it should be noted that they present error statistics as a mean value per model category (these categories are defined in terms of processes represented), and not for individual models (which may perform better than the average of the

model category they are in). Yet, at least it can be stated that the performance of our model is at least as good as the mean of any the model categories considered in Best and Grimmond (2012). When considering the mean bias error on the simulated sensible heat flux, which for *UrbClim* is 10 W m^{-2} , we find that the performance of *UrbClim* also ranks with the best of the model-class mean values presented in Best and Grimmond (2012), which range from 11 to 74 W m^{-2} . When comparing these figures, it is important to keep in mind that, in our model, we did not employ locally measured forcing data as was done in the off-line simulations. Instead, in our approach the land surface scheme is fully coupled to the atmospheric scheme described in Section 2.2, which is itself coupled to output fields of the ECMWF model.

A striking aspect is the systematically positive bias for simulated sensible heat, both in our results over Toulouse and in the validation results for Melbourne presented in Best and Grimmond (2012). While this could be a deficiency shared by all models, it could also suggest that eddy-correlation measurements over urban areas yield systematically low sensible heat flux values. This appears to be supported by findings of Sakai et al. (2001), who observed that, over rough surfaces, and depending on the averaging time used, a considerable share (up to 17%) of the turbulent heat flux could be ‘lost’ because of the undersampling of large eddies. Finnigan et al. (2003) equally found that, over rough surfaces, turbulent energy fluxes may be systematically underestimated by 10-15%.

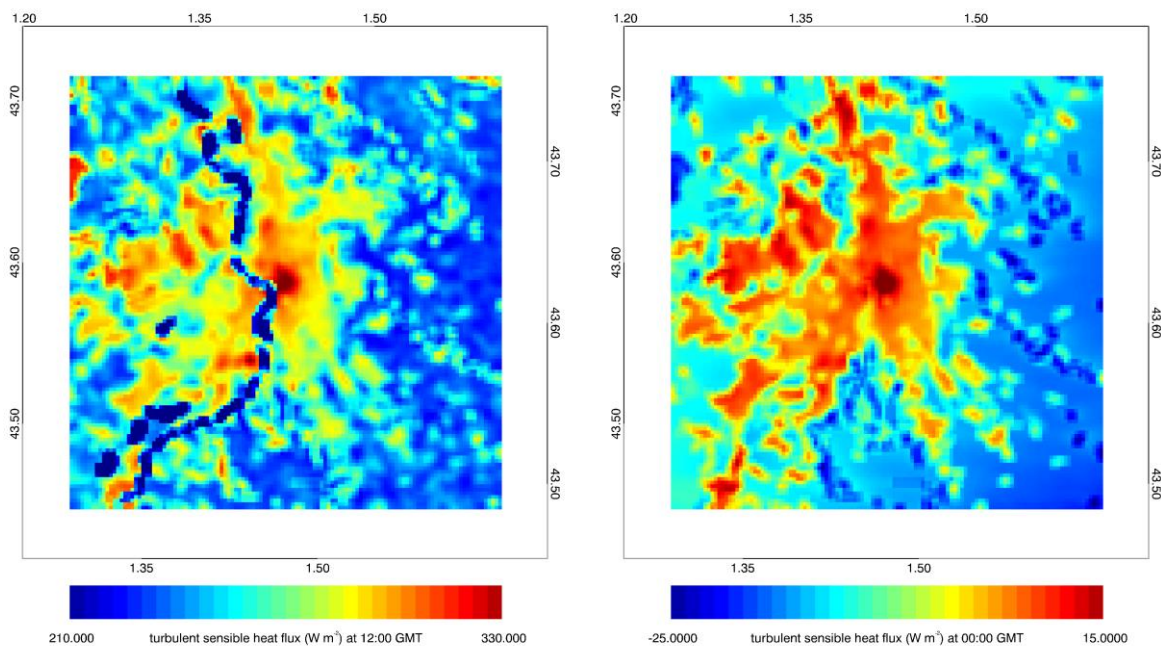


Figure 5. Simulated average 12:00 UT (left) and 00:00 UT (right) surface turbulent sensible heat flux for Toulouse and surroundings, for the period June-July 2004.

When further comparing the error statistics of the simulated energy fluxes with other results presented in the literature, we found our results to be in the same range as those obtained with more sophisticated models (see error statistics presented, e.g., in Lac et al., 2008; Ryu et al., 2011; Loridan et al., 2013; Bueno et al., 2013), although the comparison with these other works is less straightforward given the different periods and site characteristics considered.

Figure 5 shows the average (for June-July 2004) surface turbulent sensible heat flux for the Toulouse area for noon and midnight conditions. The core of the city stands out very clearly, with an average noon-time urban-rural difference of this flux amounting to approximately 120 W m^{-2} ; at night the difference is around 40 W m^{-2} . During the day, the Garonne river crossing through Toulouse also has a distinct signature with low sensible heat flux values.

3.2 Ghent

As a second test case, the model was applied on a domain centred on Ghent, a medium-sized city in the North of Belgium with approximately 250,000 inhabitants. The spatial patterns of land cover type and vegetation cover fraction of the domain are shown in Figure 6, from which it can be seen that the city has a relatively small dense urban core surrounded by less densely built-up cover. The rural areas surrounding the city are composed of agricultural crop fields interspersed with grassland and a few small scattered forests. A major industrial and harbour area extends to the north of the city. The period selected for the simulation is the month of August 2012, the choice of which was motivated by the availability of relevant measurements from an experimental campaign. This period is characterized by fairly regular Summer weather with a short episode of relatively high (for Belgium, that is) temperatures, climbing to 34°C .

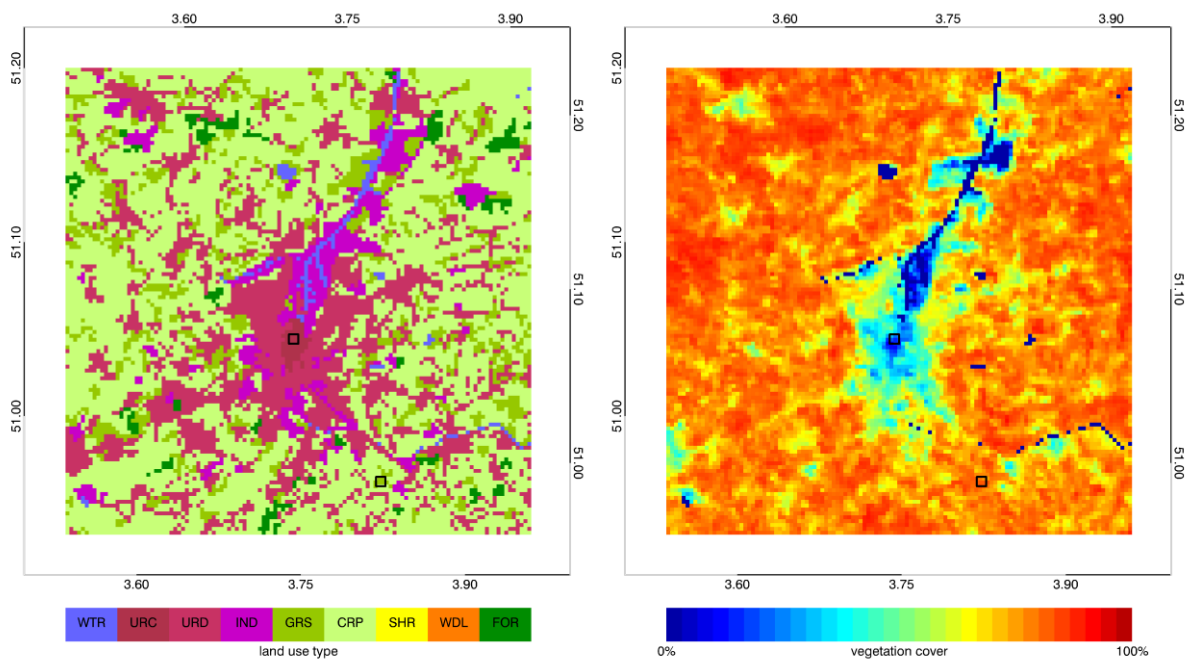


Figure 6. Spatial distribution of the dominant land cover type (left) and percentage vegetation cover (right) for the Ghent modelling domain. The acronyms denoting the different land cover types are explained in Table 1.

The focus of this validation was on the model's ability to reproduce observed urban-rural air temperature differences. (This may seem of obvious interest in urban heat island studies but, somewhat surprisingly, we found that relatively few modelling studies actually consider this quantity.) Temperature was measured by means of an Onset HOB0 U23-002 Pro v2 temperature data logger mounted inside a Young 43502 radiation shield with active ventilation. This combination

yields a temperature measuring device with a specified accuracy of the order of 0.2°C , even under conditions of strong insolation and low ambient ventilation speed. Urban temperature measurements were acquired in a courtyard surrounded by buildings of approximately 15 m height, in an area that is fairly uniform over hundreds of metres in terms of the urban canopy's height-width ratio. Measurements were done at a height of 4 m above the courtyard's concrete floor. Rural temperature observations were obtained at a grassland site approximately 10 km South-East from the city centre, at an experimental farm near the locality of Melle. The positions of the measurement stations within the domain are displayed in Figure 6.

Temperature was measured at a height of approximately 1.8 m above a field of short grass. An estimate of the instrument's accuracy was made by comparing a time series of measured temperature with that of a nearby (200 m away) weather station operated by the Belgian Royal Meteorological Institute. This was done for the study period (August 2012), and showed a negligible bias, and a root mean square difference between both measurements of 0.43°C . This is higher than the previously mentioned accuracy of 0.2°C which, based on error propagation theory, can be partly ascribed to the fact that the error on the temperature difference between two (assumed stochastically independent) sensors is the individual error of either, multiplied by a factor $2^{1/2}$. Apart from that, the spatial separation of a few hundred metres most likely also adds to the observed difference between both measurement series. Using this root mean square difference of 0.43°C as a representative value for the overall accuracy of the temperature measurements both in the city and in the rural area, and again applying error propagation principles, the resulting accuracy of the temperature difference between the urban and rural sites is 0.61°C .

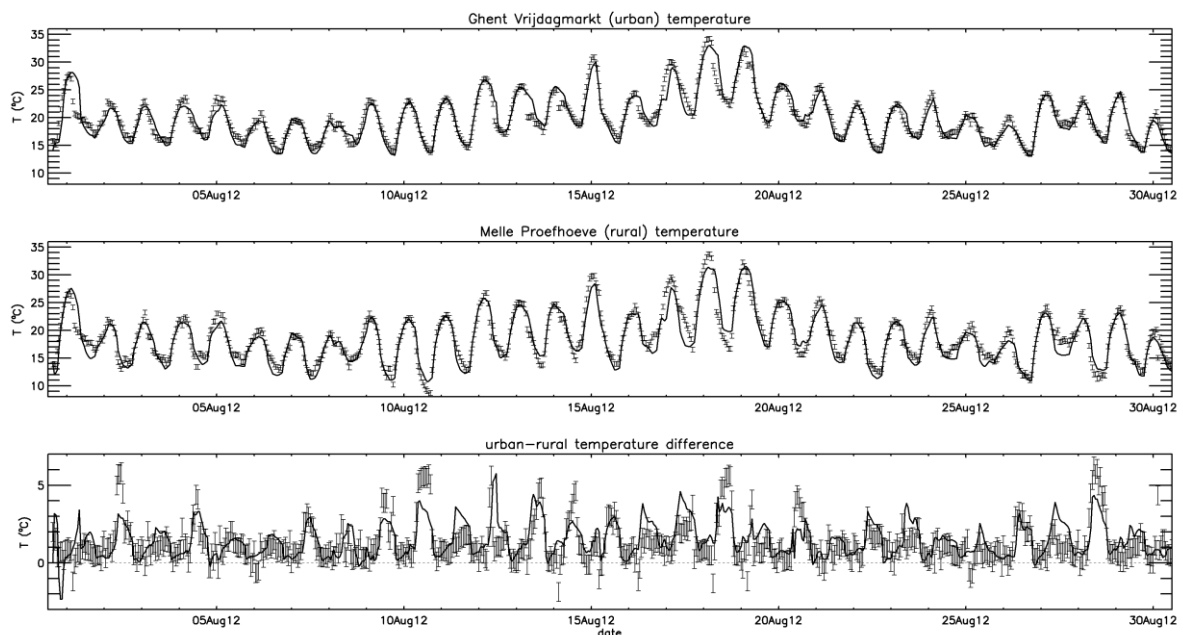


Figure 7. Simulated (solid line) and observed (error flags) surface air temperature for the climate observation stations located in central Ghent (upper panel) and the nearby rural location (middle panel), for the month of August 2012. The lower panel shows the difference of both temperature measurements as a function of time.

Figure 7 shows observed and simulated surface air temperatures together. The error flags on the observed values represent the accuracies of the temperature (difference) measurements derived above. It can be seen that the overall amplitude and phase of the simulated temperature time series

match those of the observations well, although on some nights the model fails to cool sufficiently over the rural site, thus yielding a too high rural minimum temperature. It should be noted, though, that the lesser behaviour of boundary layer models under the stable conditions at which these deficiencies occur is not uncommon and, indeed, a challenge for most weather and climate models (Holtslag et al., 2013).

Nevertheless, the error statistics point to an overall good performance of the model, with a bias of a few tenths of a degree, a root mean square error below 1.4 °C, and a correlation coefficient with value 0.95 for both sites. This puts our simple model in the same performance category as that of more detailed and complete mesoscale models (see, e.g., Bohnenstengel et al., 2011; Salamanca et al., 2011; Chemel and Sokhi, 2012; Loridan et al., 2013). Also, it yields a similar performance as that obtained with a previous (but almost identical) version of *UrbClim*'s land surface scheme, but then embedded in the full mesoscale model ARPS (Demuzere et al., 2008; Sarkar and De Ridder, 2011; Wouters et al., 2013). When comparing simulated temperature to station values, this adequate performance is of course less a merit of our model than that of the driving atmospheric fields, which in this study are taken from the ECMWF global operational model.

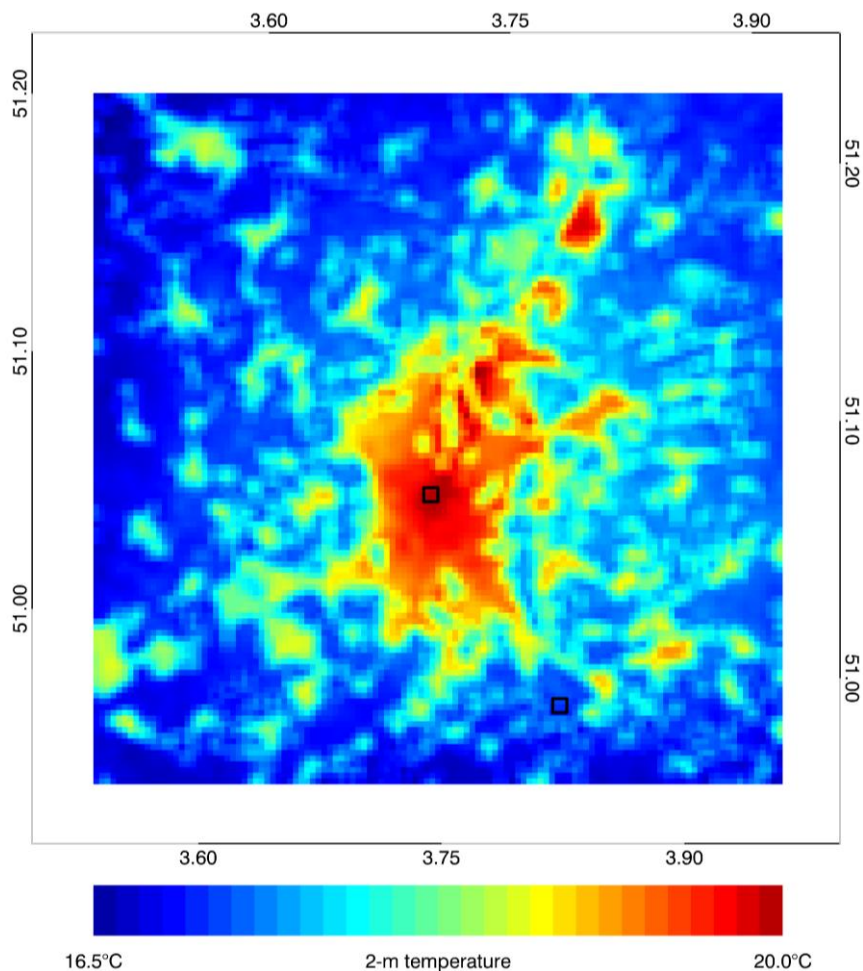


Figure 8. Simulated average 22:00 UT surface air temperature for the Ghent domain, for August 2012.

Conversely, a feature which does arise solely from our model, i.e., which is not contained at all in the meteorological driving fields, is the capacity of *UrbClim* to reproduce, as shown in the lower panel of

Figure 7, the observed urban-rural temperature differences. Clearly, this quantity is much harder to reproduce correctly, as it arises as a rather small difference of two values exhibiting a comparatively large diurnal amplitude. Nevertheless, the error statistics show a fair agreement between the simulated and observed temperature differences, with a bias of a few tenths °C, a root mean square error of 1.0 °C, and a correlation coefficient of 0.68. It should also be noted that a part of the root mean square error most likely stems from the uncertainty of the observations, which, as estimated above, amounts to 0.61°C.

On Figure 7 it can be seen that the model captures the timing of the diurnal peaks fairly well, though it underestimates the magnitude of some of the stronger ones. Analysis of the time series reveals that this is largely caused by the insufficient nocturnal cooling over the rural site, which was mentioned above. Conversely, at occasions characterized by a rather low UHI intensity the model has a tendency to slightly overestimate this intensity compared to observed values. As a result, the simulated variability of the urban heat island intensity is somewhat lower than the observed one.

A comparison of the performance of the urban-rural temperature difference simulated by *UrbClim* with that of other models is not straightforward as, to our best knowledge, this quantity is rarely ever reported in the literature. However, comparing with our own recent work (Sarkar and De Ridder, 2011; Wouters et al., 2013) in which the urban surface scheme was embedded within the full mesoscale model ARPS, it can be concluded that the error statistics for the urban-rural temperature difference are, again, fairly similar.

To end this section, in Figure 8 we show the spatial distribution of the simulated monthly mean surface air temperature at 21:00 UTC (corresponding to 23:00 local time) for August 2012. A distinct urban heat island pattern is apparent, with an amplitude of approximately 3°C.

3.3 Antwerp

The city of Antwerp, as Ghent, is located in Northern Belgium. The number of inhabitants in the city is approximately 500,000, but the wider metropolitan area counts nearly double that. Antwerp is characterized by a dense urban core surrounded by built-up areas of medium density. The area surrounding Antwerp is relatively flat, and is dominated by grassland and crop areas, and some scattered forest (Figure 9). The city is run through by the Scheldt river, and has a major harbour area in the North.

The focus of the validation for Antwerp is wind speed. Use is made of observations made at two locations. The urban site is in on top of a small building in the court yard of a school ('Koninklijk Lyceum Antwerpen') located near the city centre, the instrument being positioned at 1.8 m above the roof. This small building being much lower (4 m above the ground) than the surrounding buildings (15 to 25 m above the ground), we consider it to be within the urban canopy layer. It must be noted that the wind measurement was set up at approximately 10 m distance from a building wall, meaning that local flow distortion may limit the representativeness of this point measurement. The rural site is located on a stretch of grassland at a farm in the nearby village of Vremde, at a distance of around 12 km from Antwerp's centre and fully within a rural zone. The nearest obstacles are trees that are located at a distance of 100 m.

At both locations, the instrument used to measure wind speed is a WindSonic, which is a 2-D ultrasonic anemometer manufactured by Gill Instruments. Without any moving parts, this sensor is particularly well suited for the observation of the low wind speed values that typically occur in the urban canopy. In order to determine instrumental accuracy, prior to deploying the sensors in the field, two WindSonic devices were set up a few metres distant from each other, and their measurement response was compared during an exercise lasting several days. This yielded an average between-instrument difference of around 4 % of the observed wind speed values, the latter covering the range 0.5-1.5 m s⁻¹ (which is typical of the urban values observed). At higher wind speed values (of 12 m s⁻¹), the manufacturer specifies an accuracy of 2 %. Considering that we are measuring in the rather lower speed range (see Figure 10), we will adopt an accuracy of 4 %.

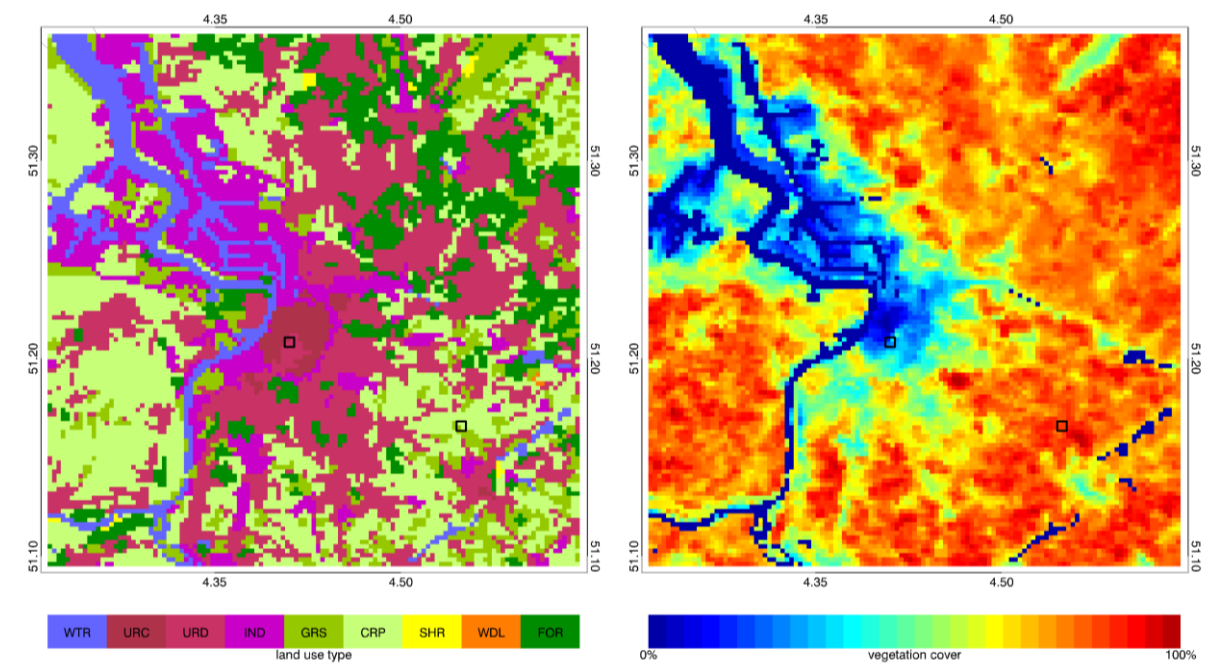


Figure 9. Spatial distribution of the dominant land cover type (left) and percentage vegetation cover (right) for the Antwerp modelling domain. The acronyms denoting the different land cover types are explained in Table 1.

An *UrbClim* simulation was conducted for the months of July-August 2013, again using a spatial resolution of 250 m, and hourly time series of wind speed were extracted from the grid cells corresponding to the two wind measurement sites. Figure 10 shows the simulated versus the observed wind speed values for the urban and rural sites. At the rural site, we found a bias of 0.25 m s⁻¹, a root mean square error of 0.64 m s⁻¹, and a correlation coefficient of 0.75. From Figure 10 it can also be seen that the rural wind speed simulation reproduces the diurnal cycle relatively correctly, apart from the daily wind speed minima, which are overestimated by the model.

At the urban site, the bias was 0.07 m s⁻¹, the root mean square error 0.49 m s⁻¹, and the correlation coefficient was found to have a low value of 0.30. It is also clear from Figure 10 that, while the wind speed magnitude is fairly well captured, most of the time the model is not capable of simulating the phase of the observed wind speed correctly. This is most likely related to microscale wind climate effects in the urban measurements, induced by the small-scale heterogeneity of the urban fabric, and which cannot be captured with 250-m size grid cells.

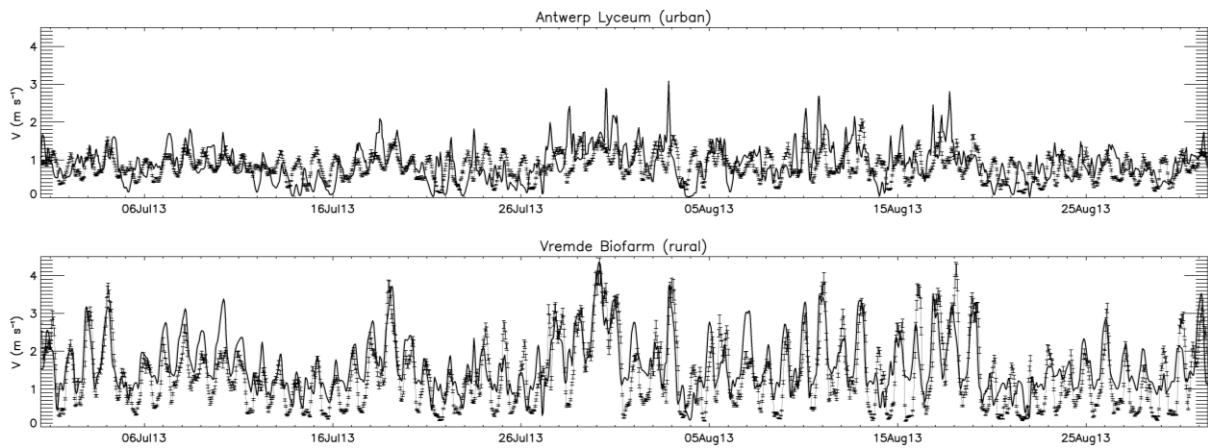


Figure 10. Simulated (solid line) and observed (error flags) wind speed for the urban and rural sites in the Antwerp domain, for the period July-August 2013.

Still, when considering error statistics obtained with full mesoscale models, as e.g. presented in Chemel and Sokhi (2012) and Loridan et al. (2013) for London, the *UrbClim* results are at least of the same level of accuracy. This is of course in part related to the quality of the forcing data. Still, *UrbClim* also reproduces fairly well the observed ratio of the urban-over-rural wind speed, a quantity which is entirely determined by the model itself, giving a simulated ratio of 0.55, against an observed value of 0.60.

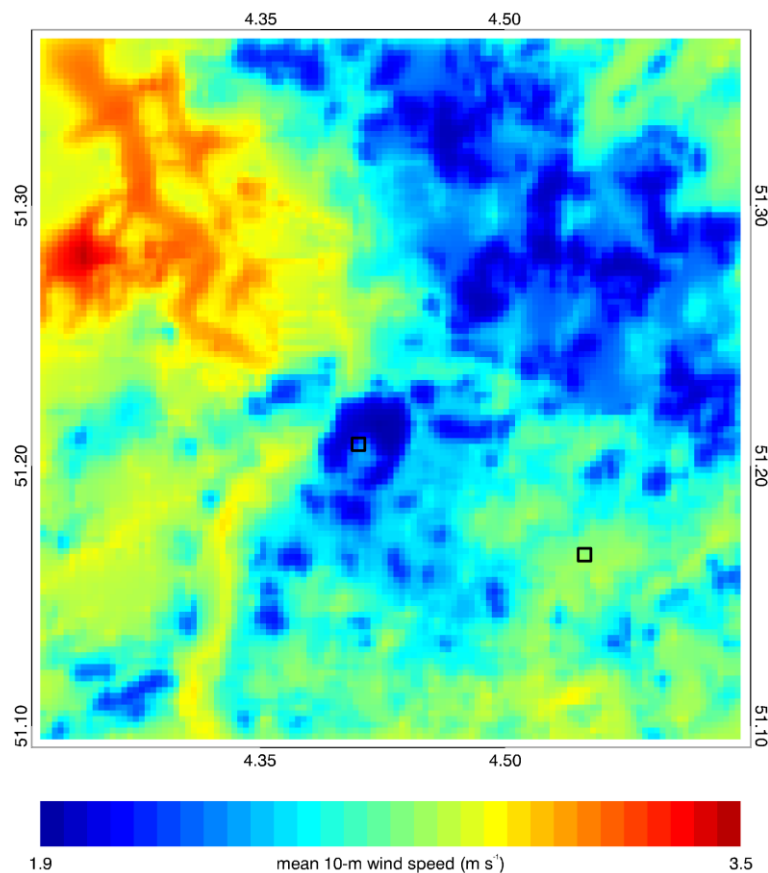


Figure 11. Simulated mean wind speed for the Antwerp domain, July-August 2013. The squares denote the positions of the wind measurement sites.

Figure 11 shows the mean 10-m wind speed for the simulation domain for July-August 2013. The city of Antwerp, as well as the forest areas in the North-East, clearly stand out as areas of low wind values. Conversely, the upper section of the Scheldt river, as well as most of the harbour and docks area in the North-Western part of the domain, are characterized by higher wind speed values, as expected.

3.4 Bilbao

Finally we conducted a validation for the area of Bilbao, located in the Basque province of Northern Spain. While the administrative area of Bilbao counts around 350,000 inhabitants, the wider metropolitan area is home to nearly 1,000,000. Bilbao, which mostly follows the valley of the Nervión river, has an elongated shape, extending from the coast inland (Figure 12). The terrain surrounding the urban area differs from that of the cities described previously by its particularly complex topography. Indeed, not only is the meteorology of this coastal city affected by the land-sea contrast, Bilbao is also surrounded by fairly steep topography, hills rising to 700 m over a horizontal distance of just 10 km. Given this, Bilbao poses a sturdy test case for the *UrbClim* model which, by the lack of an internal pressure gradient calculation, does not account at all for terrain-driven thermal atmospheric circulations.

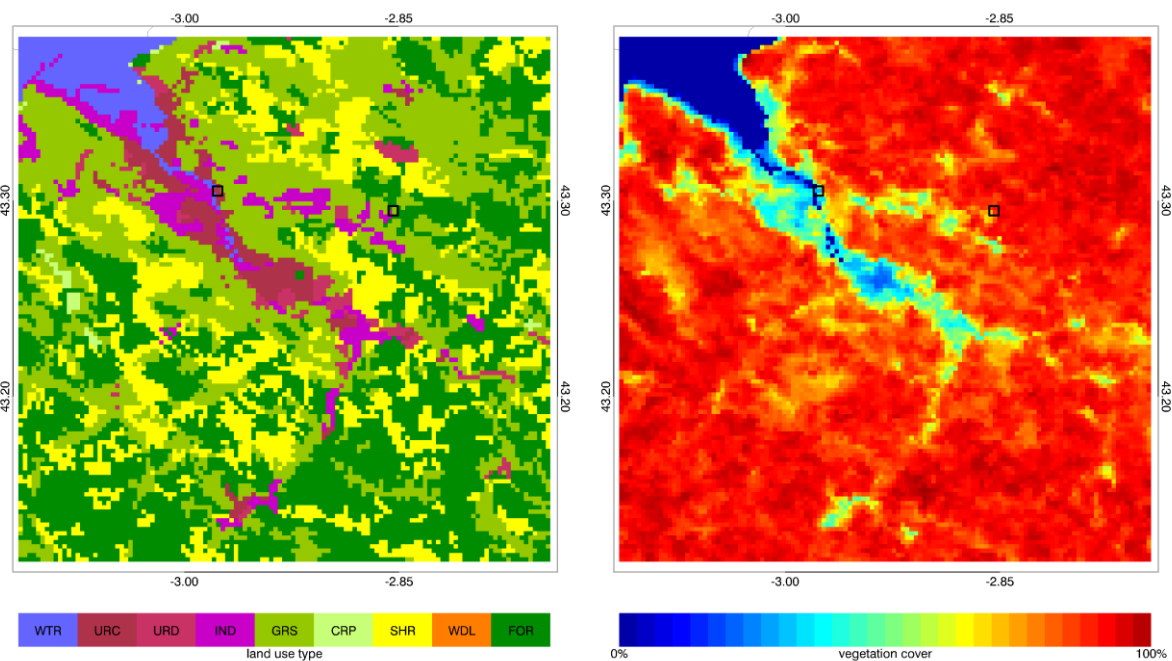


Figure 12. Spatial distribution of the dominant land cover type (left) and percentage vegetation cover (right) for the Bilbao modelling domain. The acronyms denoting the different land cover types are explained in Table 1.

In the validation we again focus on temperature, including urban-rural temperature differences (i.e., the heat island intensity). Temperature measurements were obtained from two meteorological stations: the Erandio urban station inside Bilbao (operated by the Environmental Department of the Basque Government), and the rural station of Derio located in a grassland area near Bilbao (operated by the Basque Meteorological Agency). The positions of these two stations are shown in Figure 12.

A simulation was conducted with *UrbClim* for the month of July 2009. Hourly 2-m temperature values were extracted from the model output at the positions of the meteorological stations of Erandio and Derio. In Figure 13 a comparison is made between simulated and measured temperature values. The simulated temperatures reproduce the observed values reasonably well with, for Erandio, a bias of 0.44 °C, a root mean square error of 1.28 °C, and a correlation coefficient of 0.90. For the Derio station, we find a bias of 0.43 °C, a root mean square error of 1.45 °C, and a correlation coefficient of 0.94.

Note that these values are comparable to those obtained for Ghent (see above), despite the more complex character of the terrain around Bilbao. Also, our error statistics are as good or better than those presented by González-Aparicio et al. (2013) for Bilbao for the period 13-18 July 2009, with Enviro-HIRLAM (Baklanov et al., 2008b), which is a full mesoscale model including a sophisticated building effect parameterization (BEP, Martilli et al., 2002). An obvious explanation is that the Enviro-HIRLAM simulation employed a resolution of 2.4 km, which is approximately ten times coarser than what *UrbClim* used (250 m). However, the fact that *UrbClim* can, at all, afford a much higher resolution is precisely a consequence of the simplifications made and the resulting model speed-up. One conclusion from this could be that an enhanced spatial resolution, even when it comes at the price of simplified model physics and dynamics, may be beneficial in the simulation of urban climate.

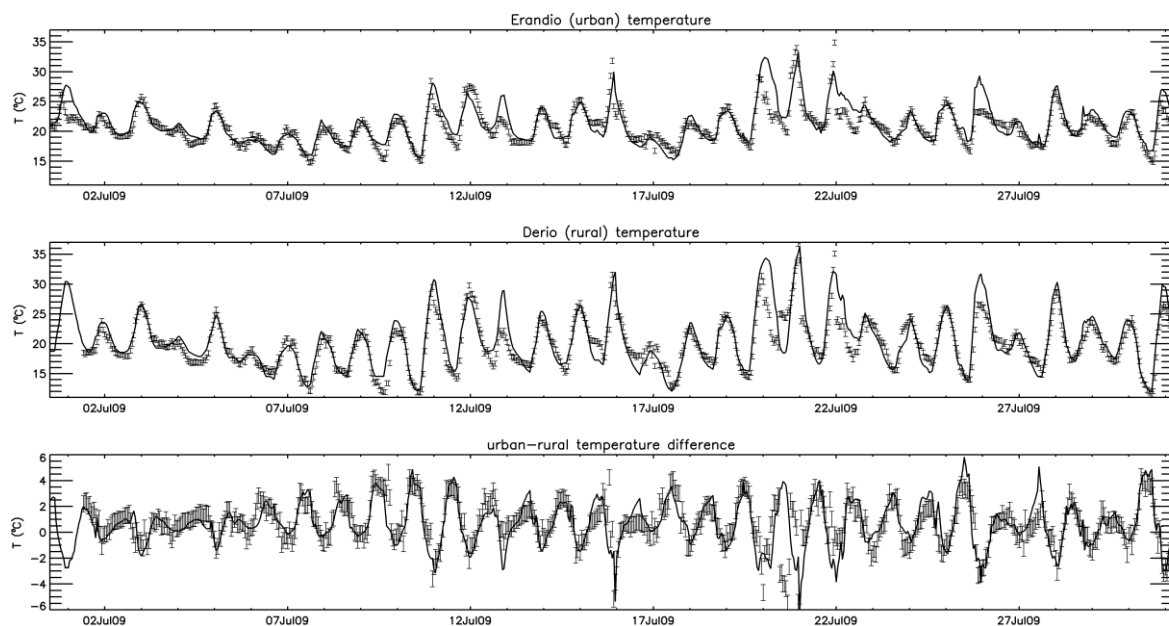


Figure 13. Simulated (solid line) and observed (symbols) surface air temperature for the climate observation stations located in Bilbao (upper panel) and the nearby rural location (middle panel), for the month of July 2009. The lower panel shows the difference of both temperature measurements as a function of time.

The model also captures the urban-rural temperature differences well, with a bias of -0.06 °C, a root mean square error of 1.27 °C, and a correlation coefficient of 0.70; again these values are not too different from the values found above for Ghent. The lower panel of Figure 13 also clearly demonstrates the ability of the model to correctly simulate the UHI intensity between Erandio and Derio, including at those instances characterized by atypical negative values, and which are most likely related to Erandio's position at the edge of Bilbao's built-up area (see Figure 12).

Figure 14 shows the 2-m temperature at 20:00 GMT, averaged for July 2009. In order to remove the topographic effects on the temperature field (which obscure the urban heat island effect), a lapse rate correction of 6.5 °C km^{-1} was applied. The resulting map shows a relatively modest UHI with an intensity of approximately 2.4 °C . The proximity of the sea (and the associated higher wind speed values), as well as the particular slender shape of the city, may be an explanation for this.

4. Discussion and conclusions

We presented a new urban climate model, composed of a simple parameterisation of the urban surface energy balance coupled to a model of the atmospheric boundary layer. It was shown that, despite the considerable simplifications made, our model is fairly well capable of reproducing observed turbulent energy fluxes, wind speed, and urban-rural air temperature differences. Error statistics of simulation results obtained for Toulouse, Ghent, Antwerp, and Bilbao point at a model performance comparable to that of more sophisticated models, such as full mesoscale models containing detailed urban canopy physics.

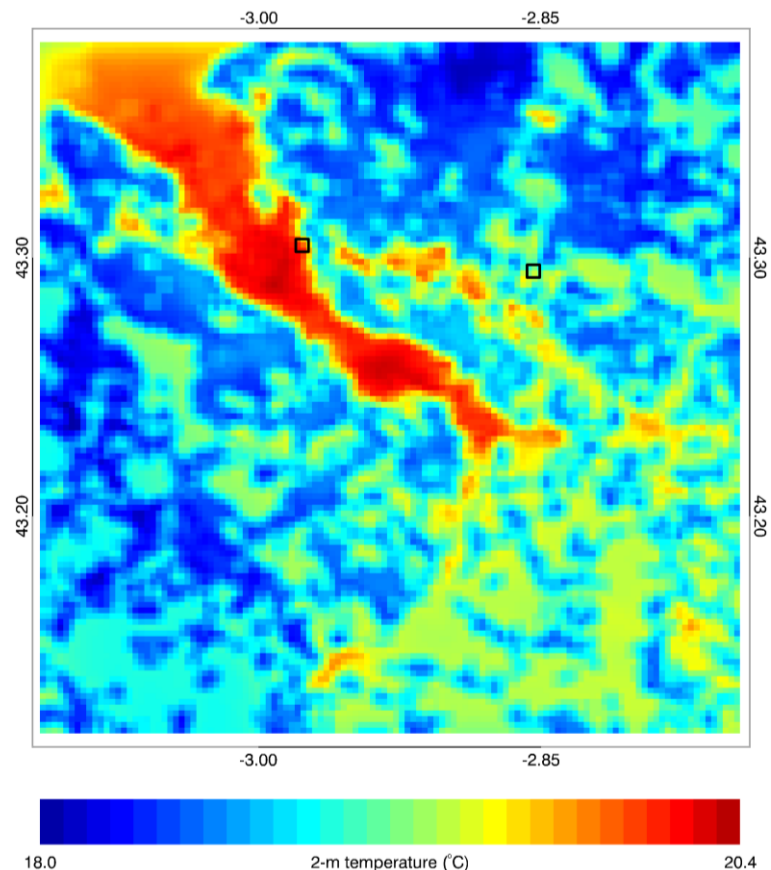


Figure 14. Simulated average 20:00 UT surface air temperature for the Bilbao domain, for the period July 2009.

At the same time, our model is very fast compared to those models. With *UrbClim*, a simulation of a Summer season extending from May to September takes approximately two days on a single computer processor, which is more than two orders of magnitude faster than a mesoscale model run in a similar configuration. The gain in execution speed observed in *UrbClim* is due to several reasons.

First, the model does not calculate the pressure gradient as a function of internal variables; instead, this quantity is prescribed from the large-scale forcing fields. This leads to a considerable gain in execution speed. Indeed, most mesoscale models operating at km-scale resolution being non-hydrostatic, they either solve a computationally costly Poisson equation to diagnose pressure (anelastic models), or they need to drastically reduce the time step to solve that portion of the dynamics permitting acoustic waves as a solution (compressible models). In either case, the resulting decrease in execution speed is considerable. In *UrbClim*, the main limitation on the time step is that enforced by the Courant criterion (27) for the numerical solution of advection. This, together with a relatively low model top and associated low maximum wind speed, generally allows a fairly long time increment. Apart from this, a more obvious reason why the *UrbClim* model is fast is that many processes occurring in the atmosphere, such as radiation transfer and cloud/precipitation physics, are not treated internally; instead the involved quantities (surface downwelling radiation, precipitation) are taken from the large-scale forcing model.

Obviously, this speed of execution comes at a price. In particular, the omission of the calculation of the pressure gradient as a function of the internal variables inhibits the development of local thermal circulations, in particular the city breeze. Observations have shown the existence of a convergent flow over urban areas, caused by the excess sensible heat flux occurring over such areas. For instance, Hidalgo et al. (2008) observed locally induced wind speeds of the order of 1.5 m s^{-1} over Toulouse. Baik (1992), in an idealized numerical simulation, found a comparable breeze strength. Lu et al. (1997), based on laboratory experiments, obtained the following scaling expression for the wind speed V_s associated with the nocturnal heat island circulation strength:

$$V_s = \left(\frac{g}{\theta} D \overline{w'\theta'} \right)^{1/3}, \quad (28)$$

with D the diameter of the area containing a perturbation kinematic heat flux $\overline{w'\theta'}$, g the gravitational acceleration, and θ a reference temperature. For a city with $D \approx 10 \text{ km}$, and assuming a heat flux perturbation of 40 W m^{-2} (as in our results for Toulouse, see Figure 3) we obtain a value of $V_s \approx 2.2 \text{ m s}^{-1}$. For daytime conditions, Hidalgo et al. (2010) suggest the following scaling:

$$V_s = \left(\frac{g}{\theta} z_i \overline{w'\theta'} \right)^{1/3}, \quad (29)$$

with z_i the convective mixing layer height. Assuming a sensible heat perturbation over the city with magnitude of 120 W m^{-2} (again taken from our result over Toulouse), and a mixing layer of 1500 m deep, a value of $V_s \approx 1.7 \text{ m s}^{-1}$ is found. Now, the values just derived refer to an overall velocity scale of the circulation. The *actual* maximum wind speed occurring in a breeze circulation generally does not exceed 60 % of this value (Baik, 1992; Lu et al., 1997), thus roughly leading to maximum wind speed values in the range of 1 to 1.5 m s^{-1} , which is fairly close to the observed and simulated values mentioned before.

Likewise, other thermal circulation systems such as the sea breeze, and anabatic and katabatic winds, cannot be simulated by *UrbClim*, which constitutes a potential limitation. It is of course very difficult to make an a priori estimate of how this omission of internal pressure gradient calculations affects the results. For that reason, we conducted several validation exercises (Section 3). The results of

these exercises show that *UrbClim* is capable of reproducing observed quantities (surface energy fluxes, wind speed, temperature) as well as any full mesoscale model containing urban surface physics; at least for the domains and periods considered here. In particular, when applied over the highly complex terrain of Bilbao, which contains a sea-land boundary as well as steep topography, our model was as accurate or better than a full mesoscale model applied over the area.

In conclusion, it is fair to say that the accuracy of *UrbClim* is at least at the level of more detailed models, yet at a fraction of the computational cost. When no detailed information regarding the urban canopy layer (separate wall and roof temperatures, in-canopy turbulence profiles, etc...) is required, or when only limited data regarding canopy geometry and material characteristics is available, we believe that a simple model as the one presented here constitutes a useful alternative for use in urban climate studies. This is particularly true when considering the execution speed of *UrbClim* compared to that of traditional 'urbanized' regional climate models, set against the rather long time integrations required to generate urban climate projections and/or scenario simulations, which are increasingly needed as a support tool to address urban climate vulnerability and adaptation issues.

We would like to emphasize that we do not want in any way to diminish the role of the more sophisticated urban canopy layer and mesoscale weather and climate models. Indeed, gaining insight into the detailed structure and mechanisms of urban canopy-layer climate and local circulation patterns can only be achieved with such sophisticated and comprehensive models. However, in the case of applied studies, e.g., aiming at establishing urban temperature maps, the level of detail can be reduced considerably without a serious loss of accuracy, and with the benefit of a large increase in model speed. With respect to the latter, the execution speed of *UrbClim* is such that it brings urban climate projections within the realm of what is feasible with current computing power. Given a modest-sized computer cluster with a few tens of CPUs, and considering that different simulation periods can be distributed over different processors, *UrbClim* is capable of performing simulations covering tens of Summer seasons, while accounting for several scenarios of climate forcing and urban land use change, and all of that within a matter of days to weeks of wall clock time.

Finally, we would like to stress the generic character of the *UrbClim* model, in the sense that, in principle, it can be configured very easily for any city. Indeed, when considering European cities, use can be made of generic and freely available data sets, including CORINE Land Cover and Urban Soil Sealing which have a spatial resolution of 100 m, and are available from the European Environment Agency (www.eea.europa.eu). When considering domains outside Europe, use can be made of 300-m GlobCover data, which is distributed by the European Space Agency (due.esrin.esa.int), or 500-m resolution MODIS Land Cover Type data (distributed by the Land Processes Distributed Active Archive Center, data available through lpdaac.usgs.gov). The latter also provides global satellite NDVI data, used to specify vegetation abundance, at a spatial resolution of 250 m, from the MODIS instrument onboard the Terra and Aqua platforms. A potential alternative data source for the NDVI is the recently launched PROBA-V instrument (Dierckx et al., 2014), which has just started generating global vegetation parameters at 300 m resolution, data of which can be obtained from VITO – the Flemish Institute for Technological Research (proba-v.vgt.vito.be). The terrain elevation data used here also has a global coverage, comes at a spatial resolution of approximately 250 m, and is available from the U.S. Geological Survey (topotools.cr.usgs.gov).

With respect to the availability of large-scale meteorological forcing data, the situation is also favourable. The data from the Operational Model of the ECMWF which have been used for this paper are available for research purposes (www.ecmwf.int). Moreover, *UrbClim* has been successfully coupled to meteorological fields contained in the freely accessible ERA-Interim archive (see apps.ecmwf.int) of the ECMWF, which is available for the whole globe at a spatial resolution of 0.75° in latitude and longitude, and covering the period from 1979 onwards at three-hourly time steps.

Despite the lack of in-canopy detail, *UrbClim* does reproduce observed canopy temperature and wind speed rather well. On the other hand, this lack of canopy level detail obviously constitutes a constraint for the evaluation of urban climate adaptation measures that act at the level of the building facets (implementation of, e.g., green roofs, white walls, ...). Therefore, future work will focus on extending the model, keeping the kB^{-1} framework, but introducing a disaggregation of the surface-atmosphere aerodynamic resistance (see Section 2) over the different facades composing the urban fabric (roof, wall, road). Work by Sugawara et al. (2009) provides evidence as to how this disaggregation can be achieved. It should be noted that the increase in the complexity of the surface physics, which would be the result of this upgrade, would most likely have little impact on the execution speed of the model taken as a whole, since the speed of *UrbClim* depends largely on the atmospheric boundary-layer module and less on the surface scheme.

Acknowledgements

The work described in this paper has received funding from the European Community's 7th Framework Programme under Grant Agreements Nos. 308497 (RAMSES) and 308299 (NACLIM), and from the Belgian Science Policy Office through its Science for a Sustainable Development Programme under contract SD/CS/041 (MACCBET). We would also like to acknowledge the CAPITOUL team for providing flux measurements over Toulouse, and the Basque Meteorological and Environmental Agencies for providing temperature measurements for Bilbao.

Appendix. Numerical stability of prognostic energy balance equations

In Section 2.1, prognostic equations of the form

$$C \frac{\partial T}{\partial t} = F(T), \quad (30)$$

appear, T (in K) denoting the temperature of the considered vegetation or upper soil layer, C (units of $\text{J m}^{-2} \text{K}^{-1}$) its heat capacity per unit projected ground surface, and F (in W m^{-2}) the sum of the in- and outgoing energy fluxes, which are themselves a function of temperature T .

Numerically, given the strongly non-linear character of $F(T)$, (30) is solved using a forward-in-time explicit scheme,

$$T_{n+1} - T_n = F(T_n) \Delta t / C, \quad (31)$$

with n the temporal index and Δt the time increment.

For this scheme to remain stable, it is required that, for a given forcing function $F(T)$, the resulting temperature increments do not increase with time, or

$$-1 \leq \frac{T_{n+2} - T_{n+1}}{T_{n+1} - T_n} \leq 1. \quad (32)$$

Using (31), and developing $F(T_{n+1})$ in a Taylor series to first order,

$$F(T_{n+1}) \approx F(T_n) + \frac{\partial F}{\partial T} (T_{n+1} - T_n), \quad (33)$$

(32) reduces to

$$-1 \leq 1 + \frac{\Delta t}{C} \frac{\partial F}{\partial T} \leq 1. \quad (34)$$

We now consider the two inequalities contained in this expression. First, the right-hand inequality leads to the requirement that

$$\frac{\partial F}{\partial T} \leq 0, \quad (35)$$

which is always the case for the energy fluxes considered (sensible, latent, longwave radiation), i.e., all other things being equal, increasing the temperature of the medium considered (leaf, urban slab or soil layer) will result in increased outgoing fluxes (energy loss of the medium).

The left-hand inequality is found to yield the requirement that

$$\Delta t \leq \frac{2C}{|\partial F / \partial T|}. \quad (36)$$

Assuming that the aerodynamic resistance r_{ah} does not vary too rapidly with temperature, the denominator of (36) can be written as

$$\begin{aligned}\frac{\partial F}{\partial T} &= \frac{\partial H}{\partial T} + \frac{\partial LE}{\partial T} + \frac{\partial R_n}{\partial T} \\ &\approx \frac{\rho_a c_p}{r_{ah}} + \frac{\rho_a L_v}{r_{ah}} \frac{\partial q_s}{\partial T} + 4\varepsilon\sigma T^3,\end{aligned}\tag{37}$$

the symbols occurring here having been explained in Section 2.1. The calculation of $\partial q_s/\partial T$ involves the use of the Clausius-Clapeyron equation. The calculation of the terms occurring in (37) and the resulting time increment is done every time step again.

However, it was found that, using (36) as a criterion in the model, stability was indeed achieved but, still, spurious saw tooth-like ('flip-flop') time patterns could arise occasionally, with alternatingly too high and low values, spoiling the solution with a non-negligible amplitude. Therefore, we considered a more stringent stability criterion, requiring that Δt be smaller than the e -folding time associated with (30).

This e -folding time can be found by re-writing (30) for a given initial temperature T_0 , and developing its right-hand side in a first-order Taylor series,

$$C \frac{\partial T}{\partial t} = F(T_0) \approx F(T_0) + \frac{\partial F}{\partial T} (T - T_0),\tag{38}$$

which, considering that $\partial F/\partial T \leq 0$, can be integrated to

$$T(\Delta t) - T_0 = \frac{F(T_0)}{|\partial F/\partial T|} \left[1 - \exp\left(-\left|\frac{\partial F}{\partial T}\right| \frac{\Delta t}{C}\right) \right],\tag{39}$$

from which the e -folding time, hence the maximum allowable (stable and flip-flop-free) time step, can be identified as

$$\Delta t \leq \frac{C}{|\partial F/\partial T|},\tag{40}$$

which is precisely half the value found earlier in (36), and which guarantees a smooth solution to (30).

Finally, in order to account for the neglect of the temperature dependence of r_{ah} in the calculation of $\partial F/\partial T$ (see above) we apply a further factor $\frac{1}{2}$ to (40) to achieve a final stable time step. Extensive testing of this criterion for the prognostic temperature equations presented in Section 2.1 has revealed its robust character.

References

- Arya SP, 2001. *Introduction to micrometeorology, 2nd edition*. Academic Press, San Diego, 420 pp.
- Baklanov, A., P. Mestayer, A. Clappier, S. Zilitinkevich, S. Joffre, A. Mahura, N.W. Nielsen, 2008a. Towards improving the simulation of meteorological fields in urban areas through updated/advanced surface fluxes description, *Atmos. Chem. Phys.*, **8**, 523-543.
- Baklanov A., U. Korsholm, A. Mahura, C. Petersen, and A. Gross, 2008b. ENVIRO-HIRLAM: on-line coupled modelling of urban meteorology and air pollution. *Adv. Sci. Res.*, **2**, 41–46.
- Best, M.,J., and C. S. B. Grimmond, 2013. Analysis of the seasonal cycle within the first international urban land-surface model comparison. *Boundary-Layer Meteorol.*, **146**, 421-446.
- Bohnenstengel, S. I., S. Evans, P.A., Clark, and S.E. Belcher, 2011. Simulations of the London urban heat island. *Q.J.R. Meteorol. Soc.*, **137**, 1625-1640.
- Brutsaert, W., 1975. The roughness length for water vapour, sensible heat, and other scalars. *J. Atmos. Sci.*, **32**, 2028– 2031.
- Bueno, B., Norford, L., Hidalgo J., and Pigeon G., 2013. The urban weather generator. *Journal of Building Performance Simulation*, **6**, 1-13.
- Chemel, C., and R.S. Sokhi, 2012. Response of London's urban heat island to a marine air intrusion in an easterly wind regime. *Boundary-Layer Meteorol.*, **144**, 65-81.
- Chen, F., R. Bornstein, S. Grimmond, J. Li, X. Liang, A. Martilli, S. Miao, J. Voogt, and Y. Wang, 2012: Research Priorities in Observing and Modeling Urban Weather and Climate. *Bull. Amer. Meteor. Soc.*, **93**, 1725–1728.
- Cheng, Y., and W. Brutsaert, 2005. Flux-profile relationships for wind speed and temperature in the stable atmospheric boundary layer. *Boundary-Layer Meteorol.*, **114**, 519-538.
- Crank, J., and Nicolson, P., 1947. A practical method for numerical evaluation of solutions of partial differential equations of the heat conduction type. *Proc. Camb. Phil. Soc.*, **43**, 50–67.
- Danielson, J.J., and D.B. Gesch, 2011. *Global multi-resolution terrain elevation data 2010 (GMTED2010)*. U.S. Geological Survey Open-File Report 2011–1073, 26 p.
- Davies, F., D. R. Middleton, and K. E. Bozier, 2007. Urban air pollution and measurements of boundary layer height. *Atmos. Environ.*, **41**, 4040 - 4049.
- Defraeye, T., Blocken, B., Carmeliet, J., 2010. CFD analysis of convective heat transfer at the surfaces of a cube immersed in a turbulent boundary layer. *International Journal of Heat and Mass Transfer*. **53**, 297–308.
- Demuzere, M., K. De Ridder, and N. van Lipzig, 2008. Modelling the energy balance in Marseille: Sensitivity to roughness length parameterizations and thermal admittance, *J. Geophys. Res.*, **113**, doi:10.1029/2007JD009113.
- De Ridder, 1997. Radiative transfer in the IAGL land surface model. *J. Appl. Meteorol.*, **36**, 12-21.

- De Ridder, 2006. Testing Brutsaert's temperature roughness parameterization for representing urban surfaces in atmospheric models. *Geophysical Research Letters*, **33**, doi:10.1029/2006GL026572.
- De Ridder, K., and G. Schayes, 1997. The IAGL Land Surface Model, *J. Appl. Meteorol.*, **36**, 167–182.
- De Ridder, K., 2010. Bulk transfer relations for the roughness sublayer. *Boundary-Layer Meteorol.*, **134**, 257-267.
- De Ridder, K., F. Lefebvre, S. Adriaensen, U. Arnold, W. Beckroege, C. Bronner, O. Damsgaard, I. Dostal, J. Dufek, J. Hirsch, L. Int Panis, Z. Kotek, T. Ramadier, A. Thierry, S. Vermoote, A. Wania, C. Weber, 2008. Simulating the impact of urban sprawl on air quality and population exposure in the German Ruhr area. Part I: reproducing the base state. *Atmospheric Environment*, **42**, 7059-7069.
- De Ridder, K., C. Bertrand, G. Casanova, and W. Lefebvre, 2012. Exploring a new method for the retrieval of urban thermophysical properties using thermal infrared remote sensing and deterministic modelling, *Journal of Geophysical Research*, **117**, doi:10.1029/2011JD017194.
- Dierckx, W., S. Sterckx, I. Benhadj, S. Livens, G. Duhoux, T. Van Achteren, M. Francois, K. Mellab, and G. Saint, 2014. PROBA-V mission for global vegetation monitoring: standard products and image quality. *Int. J. Remote Sens.*, **35**, 2589 – 2614.
- Diffenbaugh, N.S., and F. Giorgi, 2012. Climate change hotspots in the CMIP5 global climate model ensemble. *Climatic Change*, **114**, 813–822.
- Dousset, B., F. Gourmelon, K. Laaidi, A. Zeghnoun, E. Giraudet, P. Bretin, E. Maurid, and S. Vandentorren, 2010. Satellite monitoring of summer heat waves in the Paris metropolitan area. *Int. J. Climatol.*, **31**, 313–323.
- Elvidge, C.D., Baugh, K.E., Dietz, J., Bland, T., Sutton, P.C., Kroehl, H.W., 1999. Radiance Calibration of DMSP-OLS Low-Light Imaging Data of Human Settlements. *Remote Sensing of Environment*, **68**, 77-88.
- Erell, E., and T. Williamson, T., 2006. Simulating air temperature in an urban street canyon in all weather conditions using measured data at a reference meteorological station. *International Journal of Climatology*, **26**, 1671-1694.
- Fan, H., and D.J. Sailor, 2005. Modeling the impacts of anthropogenic heating on the urban climate of Philadelphia: a comparison of implementations in two PBL schemes. *Atmospheric Environment*, **39**, 73–84.
- Field, C.B., V. Barros, T.F. Stocker, D. Qin, D.J. Dokken, K.L. Ebi, M.D. Mastrandrea, K.J. Mach, G.-K. Plattner, S.K. Allen, M. Tignor, and P.M. Midgley (eds.). Cambridge University Press, Cambridge, UK, and New York, NY, USA, 582 pp.
- Finnigan, J.J., R. Clement, Y. Malhi, R. Leuning, and H.A Cleugh, 2003. A re-evaluation of long-term flux measurement techniques. Part I: averaging and coordinate rotation. *Boundary-Layer Meteorology*, **107**, 1–48.
- Gabriel K.M.A., and W.R. Endlicher, 2011. Urban and rural mortality rates during heat waves in Berlin and Brandenburg, Germany. *Env. Poll.*, **159**, 2044-2050.

- Garratt J.R., 1992. *The Atmospheric Boundary Layer*. Cambridge University Press, UK, 316 pp.
- Ghuo, X., and H. Zhang, 2007. A performance comparison between nonlinear similarity functions in bulk parameterization for very stable conditions. *Environ. Fluid Mech.*, **7**, 239–257.
- González-Aparicio, I., J. Hidalgo, A. Baklanov, U. Korsholm, R. Nuterman, A. Mahura, and O. Santa-Coloma, 2013. Urban boundary layer analysis in the complex coastal terrain of Bilbao using Enviro-HIRLAM. *Theor. Appl. Climatol.*, **113**, 511-527.
- Grimmond, C.S.B., M. Blackett, M. J. Best, J. Barlow, J.-J. Baik, S. E. Belcher, S. I. Bohnenstengel, I. Calmet, F. Chen, A. Dandou, K. Fortuniak, M. L. Gouvea, R. Hamdi, M. Hendry, T. Kawai, Y. Kawamoto, H. Kondo, E. S. Krayenhoff, S.-H. Lee, T. Loridan, A. Martilli, V. Masson, S. Miao, K. Oleson, G. Pigeon, A. Porson, Y.-H. Ryu, F. Salamanca, L. Shashua-Bar, G.-J. Steeneveld, M. Tombrou, J. Voogt, D. Young, and N. Zhang, 2010. The international urban energy balance models comparison project: First results from phase 1. *J. Appl. Meteor. Climatol.*, **49**, 1268–1292.
- Grimmond, C.S.B., M. Blackett, M. J. Best, J.-J. Baik, S. E. Belcher, J. Beringer, S. I. Bohnenstengel, I. Calmet, F. Chen, A. Coutts, A. Dandou, K. Fortuniak, M. L. Gouvea, R. Hamdi, M. Hendry, M. Kanda, T. Kawai, Y. Kawamoto, H. Kondo, E. S. Krayenhoff, S.-H. Lee, T. Loridan, A. Martilli, V. Masson, S. Miao, K. Oleson, R. Ooka, G. Pigeon, A. Porson, Y.-H. Ryu, F. Salamanca, G.J. Steeneveld, M. Tombrou, J. A. Voogt, D. T. Young and N. Zhang, 2011. Initial results from Phase 2 of the international urban energy balance model comparison. *Int. J. Climatol.*, **31**, 244–272.
- Gutman, G., and A. Ignatov, 1998. Derivation of green vegetation fraction from NOAA/AVHRR for use in weather prediction models. *Int. J. Remote Sens.*, **19**, 1533–1543.
- Hagishima, A., J. Tanimoto, and K.-I. Narita, 2005. Intercomparison of experimental convective heat transfer coefficients and mass transfer coefficients at urban surfaces. *Boundary-Layer Meteorol.*, **117**, 551-576.
- Hidalgo, J., V. Masson, and L. Gimeno, 2010. Scaling the daytime urban heat island and urban-breeze circulation. *J. Appl. Meteorol. and Climatol.*, **49**, 889-901.
- Hidalgo, J., G. Pigeon, and V. Masson, 2008. Urban-breeze circulation during the CAPITOU experiment: observational data analysis approach. *Meteorology and Atmospheric Physics*, **102**, 223-241.
- Holtslag, A.A.M., G. Svensson, P. Baas, S. Basu, B. Beare, A.C.M. Beljaars, F.C. Bosveld, J. Cuxart, J. Lindvall, G.J. Steeneveld, M. Tjernström, and B.J.H. Van De Wiel, 2013. Stable atmospheric boundary layers and diurnal cycles, challenges for weather and climate models. *Bull. Amer. Meteor. Soc.*, doi: 10.1175/BAMS-D-11-00187.1.
- Hong, S.-Y., H.-L. Pan, 1996. Nonlocal boundary layer vertical diffusion in a medium-range forecast model. *Mon. Wea. Rev.*, **124**, 2322–2339.
- Ikeda, R., and H. Kusaka, 2010. Proposing the simplification of the multilayer urban canopy model: Intercomparison study of four models. *J. Appl. Meteor. Climatol.*, **49**, 902-919.

IPCC, 2012. *Managing the Risks of Extreme Events and Disasters to Advance Climate Change Adaptation. A Special Report of Working Groups I and II of the Intergovernmental Panel on Climate Change.*

Jones, H.G., 1992. *Plants and Microclimate: A Quantitative Approach to Environmental Plant Physiology.* Cambridge University Press, Cambridge, 428 pp.

Jürges, W., 1924. *Der Wärmeübergang an einer ebenen Wand.* Beihefte zum, Gesundheits-Ingenieur vol. 19, Druck und Verlag von R. Oldenbourg, 52 pp.

Kanda M., M. Kanega, T. Kawai, R. Moriwaki, and H. Sugawara, 2007. Roughness lengths for momentum and heat derived from outdoor urban-scale models. *J. Appl. Meteorol. Clim.*, **46**, 1067–1079.

Lac, C., F. Bonnardot, O. Connan, C. Camail, D. Maro, D. Hebert, M. Rozet, J. Pergaud, 2008. Evaluation of a mesoscale dispersion modelling tool during the CAPITOUL experiment. *Meteorol. Atmos. Phys.*, **102**, 263–287.

Loridan, T., F. Lindberg, O. Jorba, S. Kotthaus, S. Grossman-Clarke, C. S. B. Grimmond, 2013. High Resolution Simulation of the Variability of Surface Energy Balance Fluxes Across Central London with Urban Zones for Energy Partitioning. *Boundary-Layer Meteorol.*, DOI 10.1007/s10546-013-9797-y.

Lu, J., S. P. Arya, W. H. Snyder, and R. E. Lawson, 1997. A laboratory study of the urban heat island in a calm and stably stratified environment. Part II: Velocity field. *J. Appl. Meteorol.*, **36**, 1392–1402.

Martilli A., A. Clappier, and M. Rotach, 2002. An urban surface exchange parameterisation for mesoscale models. *Boundary-Layer Meteorol.*, **104**, 261–304.

Masson, V., 2000. A physically-based scheme for the urban energy budget in atmospheric models. *Boundary-Layer Meteorol.*, **94**, 357–397.

Masson, V., L. Gomes, G. Pigeon, C. Lioussé, V. Pont, J.-P. Lagouarde, J. Voogt, J. Salmond, T. R. Oke, J. Hidalgo, D. Legain, O. Garrouste, C. Lac, O. Connan, X. Briottet, S. Lachéradé, P. Tulet, 2008. The Canopy and Aerosol Particles Interactions in Toulouse Urban Layer (CAPITOUL) experiment. *Meteorol. Atmos. Phys.*, **102**, 135–157.

Mauder, M., S.P. Oncley, R. Vogt, T. Weidinger, L. Ribeiro, C. Bernhofer, T. Foken, W. Kohsiek, H.A. R. De Bruin, H. Liu, 2007. The energy balance experiment EBEX-2000. Part II: Intercomparison of eddy-covariance sensors and post-field data processing methods. *Boundary-Layer Meteorol.*, **123**, 29–54.

Nakamura, Y. and T.R. Oke, 1988. Wind, temperature and stability conditions in an E-W oriented urban canyon, *Atmospheric Environment*, **22**, 2691-2700.

Oke, T.R., 2002. *Boundary layer climates.* Taylor & Francis, 464 pp.

Oleson, K. W., G. B. Bonan, J. Feddema, M. Vertenstein, and C. S. B. Grimmond, 2008a. An urban parameterization for a global climate model. 1. Formulation and evaluation for two cities. *J. Appl. Meteorol. Climatol.*, **47**, 1038–1060,

- Paulson, C. A., 1970: The mathematical representation of wind speed and temperature profiles in the unstable atmospheric surface layer. *J. Appl. Meteorol.*, **9**, 857–861.
- Physick W.L., and J.R. Garratt, 1995. Incorporation of a high-roughness lower boundary into a mesoscale model for studies of dry deposition over complex terrain. *Boundary-Layer Meteorol.*, **74**, 55–71.
- Pielke, R.A, Sr., 2002. *Mesoscale meteorological modeling. 2nd Edition*, Academic Press, San Diego, 676 pp.
- Pigeon, G.,D. Legain, P. Durand, and V. Masson, 2007. Anthropogenic heat release in an old European agglomeration (Toulouse, France). *Int. J. Climatol.*, **27**, 1969–1981.
- Pillai, S.S., and R. Yoshie, 2013. Flow velocity and temperature effects on convective heat transfer coefficient from urban canopy surfaces by numerical simulation. *Journal of Urban and Environmental Engineering*, **7**, 74-81.
- Piringer, M., S. Joffre, A. Baklanov, A. Christen, M. Deserti, K. De Ridder, S. Emeis, P. Mestayer, M. Tombrou, D. Middleton, K. Baumann-Stanzer, A. Dandou, A. Karppinen and J. Burzynski, 2007. The surface energy balance and the mixing height in urban areas – activities and recommendations of COST Action 715. *Boundary-Layer Meteorology*, **124**, 3-24.
- Porson, A., I.N. Harman, S.I Bohnenstengel, and S.E. Belcher, 2009. How many facets are needed to represent the surface energy balance of an urban area? *Boundary-Layer Meteorol.*, **132**, 107-128.
- Rockel, B., Will, A., and Hense, A. (2008). The regional climate model COSMO-CLM (CCLM). *Meteorol. Z.*, **17**, 347-348.
- Rotach, M.W., R. Vogt, C. Bernhofer, E. Batchvarova, A. Christen, A. Clappier, B. Feddersen, S.-E. Gryning, G. Martucci, H. Mayer, V. Mitev, T. R. Oke, E. Parlow, H. Richner, M. Roth, Y.-A. Roulet, D. Ruffieux, J. A. Salmond, M. Schatzmann, and J. A. Voogt, 2005. BUBBLE – an urban boundary layer meteorology project. *Theor. Appl. Climatol.*, **81**, 231–261.
- Rowley, F. B., A. B. Algren, and J. L. Blackshaw, 1930. Surface conductances as affected by air velocity, temperature, and character of surface. *ASHRAE Trans.*, **36**, 429–446.
- Ryu, Y.-H., J.-J. Baik, S.-H. Lee, 2011. A new single-layer urban canopy model for use in mesoscale atmospheric models. *J. Appl. Meteor. Climatol.*, **50**, 1773–1794.
- Sailor, D.J., Fan, H., 2004. The importance of including anthropogenic heating in mesoscale modeling of the urban heat island. Proceedings of the 84th Annual Meeting of the American Meteorological Society, Symposium on Planning, Nowcasting, and Forecasting in the Urban Zone, Seattle, WA, USA, January 2004.
- Sakai, R.K., D.R. Fitzjarrald, and K.E. Moore, 2001. Importance of low-frequency contributions to eddy fluxes observed over rough surfaces. *J. Appl. Meteor.*, **40**, 2178–2192.
- Salamanca, F., A. Martilli, M. Tewari, F. Chen, 2011. A Study of the Urban Boundary Layer Using Different Urban Parameterizations and High-Resolution Urban Canopy Parameters with WRF. *J. Appl. Meteor. Climatol.*, **50**, 1107–1128.

- Sarkar, A., and K. De Ridder, 2011. The urban heat island intensity of Paris: a case study based on a simple urban surface parameterisation. *Boundary-Layer Meteorology*, **138**, 511-520.
- Sarrat, C., A. Lemonsu, V. Masson, and D. Guedalia, 2006. Impact of urban heat island on regional atmospheric pollution. *Atmos. Environ*, **40**, 1743-1758.
- Schär, C., P.L. Vidale, D. Luthi, C. Frei, C. Haberli, M.A. Liniger, and C. Appenzeller, 2004. The role of increasing temperature variability in European Summer heat waves. *Nature*, **427**, 332-336.
- Short, C.A., M.J. Cook, and A. Woods, 2009. Low energy ventilation and cooling within an urban heat island. *Renewable Energy*, **34**, 2022-2029.
- Sobrino, J.A., R. Oltra-Carrió, G. Sòria, R. Bianchi, M. Paganini, 2012. Impact of spatial resolution and satellite overpass time on evaluation of the surface urban heat island effects. *Remote Sensing of Environment*, **117**, 50-56.
- Solazzo, E., and R.E. Britter, 2007. Transfer processes in a simulated urban street canyon. *Boundary-Layer Meteorol.*, **124**, 43-60.
- Sørensen, J.H., A. Rasmussen, H. Svensmark, 1996. Forecast of atmospheric boundary-layer height utilised for ETEX real-time dispersion modelling. *Physics and Chemistry of the Earth*, **21**, 435-439.
- Sugawara, H., and K. Narita, 2009. Roughness length for heat over an urban canopy. *Theor. Appl. Climatol.*, **95**, 291-299.
- Van Weverberg, K., K. De Ridder, and A. Van Rompaey, 2008. Modeling the contribution of the Brussels heat island to a long term temperature time series. *Journal of Applied Meteorology and Climatology*, **47**, 976-990.
- Voogt, J. A., and C. J. B. Grimmond, 2000. Modeling surface sensible heat flux using surface radiative temperatures in a simple urban area. *J. Appl. Meteor.*, **39**, 1679-1699.
- Walcek, C., 2000. Minor flux adjustment near mixing ratio extremes for simplified yet highly accurate monotonic calculation of tracer advection. *J. Geophys. Res.*, **105**, 2156-2202.
- Wouters, H., K. De Ridder, N.P.M. van Lipzig, M. Demuzere, and D. Lauwaet, 2013. The diurnal evolution of the urban heat island of Paris: a model-based case study during Summer 2006. *Atmospheric Chemistry and Physics*, **13**, 8525-8541.
- Wouters, H., M. Demuzere, K. De Ridder, N. van Lipzig, G. Vogel, 2014. Exploring water-storage and evaporation for urban impervious land cover. Submitted to *Urban Climate*.
- Xue, M., K. K. Droegemeier, and V. Wong, 2000. The Advanced Regional Prediction System (ARPS) – A multi-scale non-hydrostatic atmospheric simulation and prediction model: Part I. Model dynamics and verification, *Meteorol. Atmos. Phys.*, **75**, 161-193.